Study on hole transporting layers and their interfaces for high performance perovskite solar cells

Yoshihiko Nishihara

February 2020

Study on hole transporting layers and their interfaces for high performance perovskite solar cells

Yoshihiko Nishihara

Doctoral Program in Nano-Science and Nano-Technology

Submitted to the Graduate School of

Pure and Applied Sciences

in Partial Fulfillment of the Requirements

for the Degree of Doctor of Philosophy in

Science

at the

University of Tsukuba

Contents

Chapter I

General Introduction

1.1 Perovskite solar cells

Recent years, study of perovskite solar cells (PSCs) which contained organic-inorganic halide perovskite structure compound (Figure 1-1) as the absorbing material is achieved rapid progress. The power conversion efficiency (PCE) was reached to 25.2% equivalent to silicon solar cells in single junction devices. And further, PCE was reached to 28.0% in silicon-perovskite multi junction devices (Figure 1-2) [1]. PSCs have excellent characteristics as solar cell devices, such as high absorbance of perovskite layers. And also, PSCs are expected significant cost reducing, weight saving and employing flexible substrate due to combining with printing technology because solution processing is possible.

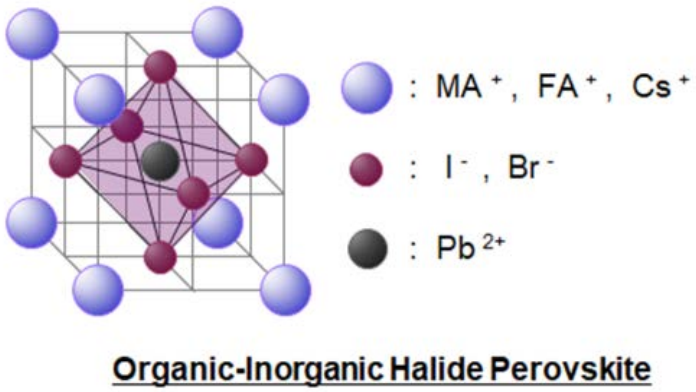

Figure 1-1. The organic-inorganic halide perovskite structure using solar cell devises

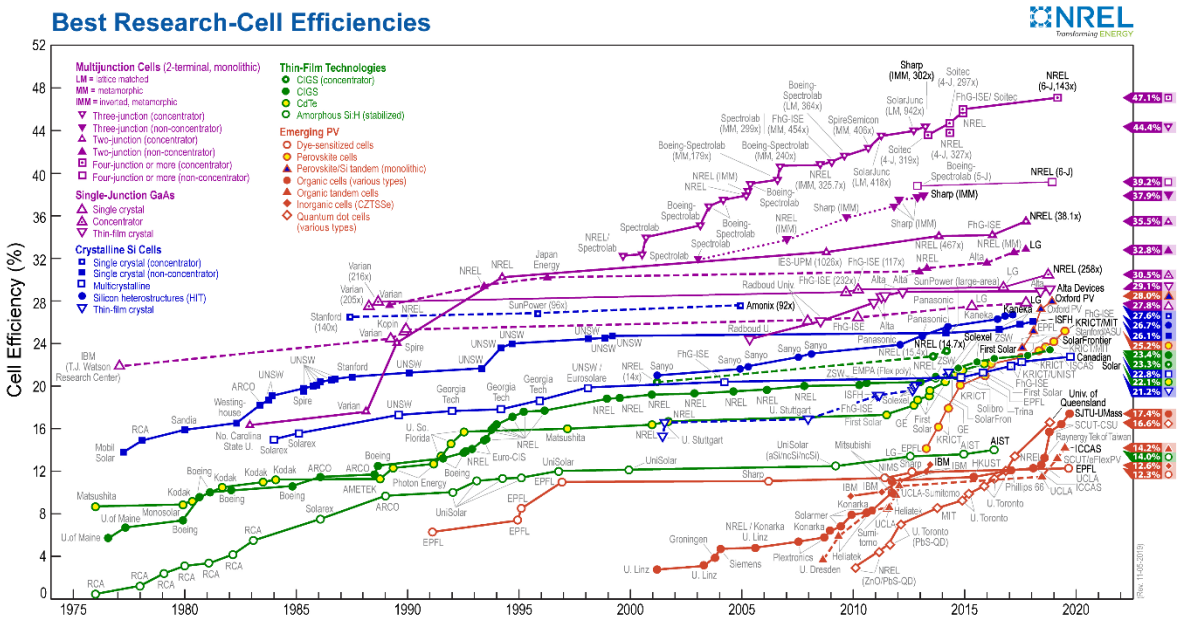

Figure 1-2. The progressing chart of best research-cell efficiency reported by the National Renewable Energy Laboratory (NREL)

1.2 Attempt to commercialize

The following cases are under way as an attempted to commercialize. Oxford Photovoltaics Limited, which achieved maximum PCE 28.0% by silicon-perovskite tandem devices (Figure 1-3(a)) in the above NREL chart, is an oxford university spin-off company. This company, which was established as a spin-out from Professor Henry Snaith's laboratory, has acquired a pilot line in 2016.[2)]

In domestic activities, the world's largest 703 cm^2 film type PSC module (Figure 1-3(b)) has been announced by New Energy and Industrial Technology Development Organization (NEDO) and Toshiba Corporation. This announced PSC module was flexible and PCE was reported at 11.7%.[3)]

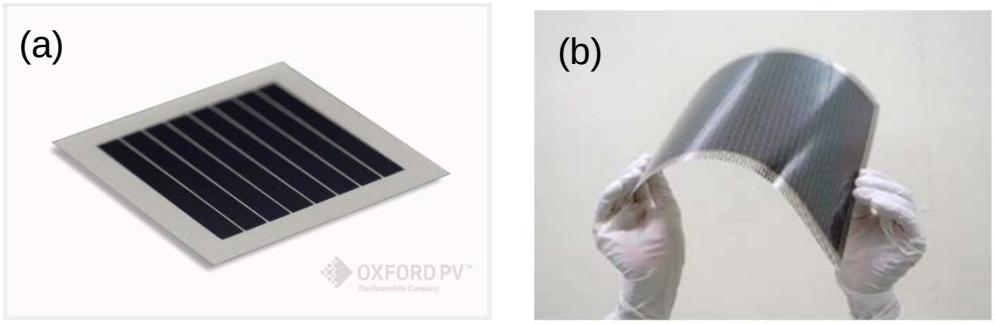

Figure 1-3. The perovskite-silicon tandem cell developed by Oxford PV (a). And the flexible perovskite solar cell module developed by NEDO and TOSHIBA (b).

As an application, PSCs were used for power supply to nodes in internet of things[4)] because of its high cost performance. These non-existent uses are also considered in the future.

1.3 Properties of organic-inorganic halide perovskite materials

Absorption spectrum of perovskite layers were depend on type and composition of halogen atoms containing the perovskite structure. In the case of $MAPbX_3$ (X = I, Br, Cl) employing methylammonium ion (MA^+) as the cation, $MAPbBr_3$ absorbs light below 550 nm. On the other hand, $MAPbI_3$ which has a wide absorption wavelength range absorbs light below 800 nm. This wavelength range covers almost all visible light. [5)]

Also, perovskite materials possess low trap densities and long carrier diffusion lengths. These diffusion lengths were reported that reached 100 nm for $MAPbI_3$ and 1000 nm for $MAPbI_{3-x}Cl_x$, which is mixed-halide perovskite material. [6)] Due to this characteristic, PCE can be increased by thickening the perovskite layer.

1.4 Device structures

The first report of PSCs was made in 2009 by Miyasaka et al. As an extension of existing dye sensitized solar cells (DSSCs).[7] Therefor, the n-i-p junction mesoporous type architecture which include mesoporous TiO_2 layer common to DSSCs (Figure 1-2(a)) is mainstream. However, the planar type architecture which was excepted TiO_2 layer requiring high-temperature process (Figure 1-2(b)) has been reported too. On the other side, the p-i-n planar type architecture (Figure 1-2(c)) which was inserted perovskite layer between p-n junctions employed at organic photovoltaic (OPV) devices has been proposed. [8), 9)]

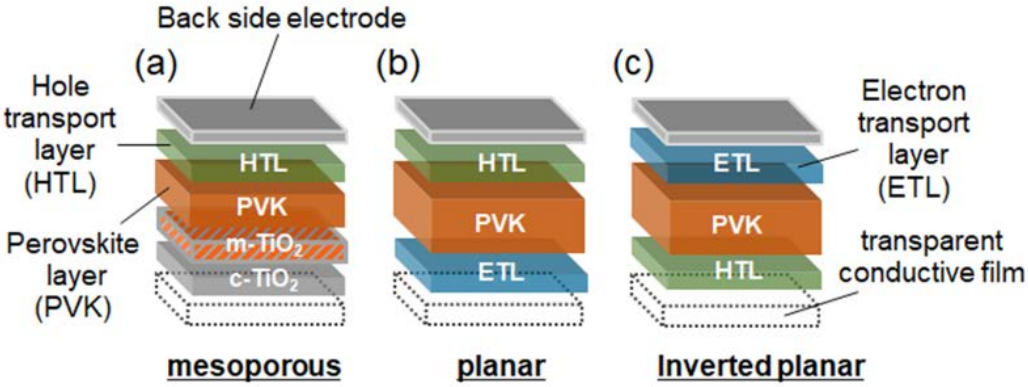

Figure 1-4. Various structures of PSC devices

Since types of solar cell used as the base are different, not only the direction of carrier transfer is reversed but also employing materials are different. In the case of mesoporous type devices, high-temperature process is inevitable when forming the TiO_2 layer. Therefore fluorine doped tin oxide (FTO) which can withstand high temperature has been employed at transparent conductive film, and substrates must have heat resistance too. On the other hand, inverted planar type devices were employed indium tin oxide (ITO) that more common transparent conductive material because low temperature process is possible, and more materials can be employed for substrates.

Metal materials employed for back side electrode are different too. In the n-i-p architecture, Au has been mainly employed. And in the p-i-n architecture, Al has been mainly employed as electrode. These electrode materials are dependent collected carrier's species (electrons or holes) and work function of the electrode material itself. When considering cost reduction and employed flexible substrates, the inverted planar type device seems more advantageous. However, the PCE tends to be higher for the mesoporous type device at the moment.

1.5 Hole Transporting Layers

Hole transporting layers (HTLs) which collect generated holes are important factor in PSCs. Therefore, various HTL materials and interface control methods such as passivation methods[10] have been explored actively.

The following properties are required for HTL materials. First, higher mobility and carrier density are desirable. Next, the valence band (VB) or the highest occupied molecular orbital (HOMO) level of the HTL materials must be close to the VB level of the perovskite material. In other words, it is necessary to consider the band alignment. Also, atmospheric stability is required because the HTL contacts the atmosphere in the n-i-p architecture.

In this doctoral study, we focused HTL materials and interface control methods. Firstly, we researched the hydrophilization treatment for inorganic HTLs in inverted planar type PSCs (Chapter II). Secondly, we researched the influence of p-type doping for organic HTLs in mesoporous type PSCs (Chapter III). Thirdly, we researched the effect of suppressing carrier recombination by inserting passivation layers (Chapter IV).

References

1) https://www.nrel.gov/
2) https://www.oxfordpv.com/
3) https://www.toshiba.co.jp/
4) S. N. R. Kantareddy, I. Mathews, S. Sun, M. Layurova, J. Yhapa, J.-P. Correa-Baena, R. Bhattacharyya, T. Buonassisi, S. E. Sarma and I. M. Peters, *IEEE Sensors Journal*, **20**, 471 (2020).
5) M. I. Saidaminov, A. L. Abdelhady, B. Murali, E. Alarousu, V. M. Burlakov, W. Peng, I. Dursun, L. wang, Y. He, G. Maculan, A. Goriely, T. Wu, O. F. Mohammed and O. M. Bakr, *Nature Communications*, **6**, 7586 (2015).
6) S. D. Stranks, G. E. Eperon, G. Grancini, C. Menelaou, M. J. P. Alcocer, T. Leijtens, L. M. Herz, A. Petrozza and H. J. Snaith, *Science*, **342**, 341 (2013).
7) A. Kojima, K. Teshima, Y. Shirai and T. Miyasaka, *J. Am. Chem. Soc.*, **131**, 6050 (2009).
8) L. Meng, J. You, T.-F. Guo and Y. Yang, *ACC. Chem. Res.*, **49**, 155(2016).
9) W. Yan, S. Ye, Y. Li, W. Sun, H. Rao Z. Liu, Z. Bian and C. Huang, *Adv. Energy. Mater.*, **6**, 1600474 (2016).
10) E. Aydin, M. D. Bastiani and S. D. wolf, *Adv. Mater.*, **2019**, 1900428(2019).

Chapter II

Influence of O_2 plasma treatment on NiO_X layer in perovskite solar cells

2.1 Introduction

There are many reports on PSCs with inverted p-i-n planar structures because of their use of a low-temperature process, their hysteresis-less behavior, and their long-term durability. [1)-7)] A NiO_x film is one of the typical hole-transporting layers (HTLs) for inverted-type PSCs. [8)-19)] The formation of the NiO_x-based HTLs has been examined by employing a sol-gel precursor solution, [10), 11)] nanoparticles, [12), 13)] spray pyrolysis, [9), 14)] electrochemical deposition, [15)] pulsed laser deposition, [16), 17)] and sputtering. [18), 19)] Wu et al. reported a high PCE of 19.19% with a device area of about 1 cm^2. [14)] However, the NiO_x-based HTL was formed by spray pyrolysis, which requires a temperature of 500 °C. Therefore, it is difficult to apply this method to the low-temperature process used to fabricate flexible solar cell modules. In our recent work, we used the NiO_x film prepared by sputtering, which can be carried out at room temperature. [18)] However, the surface of the NiO_x film fabricated by sputtering is too hydrophobic for the precursor solution to form a uniform perovskite film by spin coating.

In this work, in order to improve its wettability, the NiO_x surface was subjected to O_2 plasma treatment under various conditions. We investigated the physical properties of O_2 plasma-treated NiO_x films and the influence of the treatment on NiO_x films used as HTLs for PSCs. [20)]

2.2 Experimental procedure

As shown in Figure 2-1, solar cells with an inverted planar structure of ITO/NiO_x/perovskite/ PCBM/LiF/Al were fabricated. Before the device fabrication, ITO substrates were cleaned by O_2 plasma treatment (Harrick Plasma PCD-32G) under normal conditions (RF power: 18 W / 15 min). NiO_x films were deposited by magnetron sputtering (target: NiO) with Ar and O_2 mixed gas (with 25:5 flux ratio) flow into a chamber (vacuum pressure: 0.5 Pa). [18)] After 210 s deposition at a power of 200 W, a 10-nm-thick NiO_x film was obtained. Then, the surfaces of NiO_x films were hydrophilized by O_2 plasma treatment. The procedure was as follows. After placing the NiO_x-film-deposited ITO glass substrates in the treatment chamber, plasma was generated under a pressure of 20 Pa. Subsequently, the pressure was increased by O_2 gas flow and maintained at 600 Pa during plasma treatment. The RF powers obtained under the normal and weak conditions were 18 and 6.8 W, respectively.

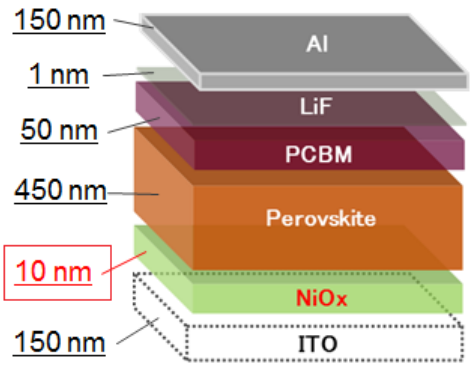

Figure 2-1. Solar cells with inverted planar structure.

Perovskite layers were formed by an anti solvent method [21] in a nitrogen-filled glovebox. The precursor solution (50 wt%) is composed of methylamine hydroiodide (MAI), lead iodide (PbI_2), and dimethyl sulfoxide (DMSO) (in the ratio 1:1:1 mol) in *N*, *N*-dimethylformamide (DMF). To form smooth perovskite films, during the spin coating of the precursor solution at 2000 rpm for 25 s a few drops of diethyl ether were added, followed by thermal annealing at 65 °C for 1 min and 100 °C for 2 min. The thickness of the obtained perovskite films was about 450 nm. After that, the electron-transporting layer (ETL) was formed by spin coating a $PC_{60}BM$ solution (20 mg/ml in chlorobenzene) at 3000 rpm for 30 s. The thickness of the ETL was about 50 nm. Finally, the 1-nm-thick LiF interlayer and 150-nm-thick Al electrode were formed by vacuum evaporation.

The current density versus voltage (*J*-*V*) characteristics of the cells were measured under dark conditions and simulated solar illumination (AM 1.5G) using a digital source meter (Keithley 2400). Incident power was calibrated using a standard silicon photovoltaic cell to match 1 sun intensity (100 mW/cm^2). The active device area with a photomask was 1.96 or 10.0 mm^2.

The surface morphology was observed by atomic force microscopy (AFM; SII NanoTechnology Nanonavi/E-sweep) in the dynamic mode. The ionization potential (IP) levels of the NiO_x films were determined by photoelectron yield spectroscopy (PYS; Bunkoukeiki BIP-KV200) in a vacuum chamber ($<5 \times 10^{-3}$ Pa). Note that all NiO_x films for IP measurement were deposited on the ITO substrate. X-ray photoelectron spectroscopy (XPS; ULVAC-PHI XPS-1800) was used to analyze the elemental composition of NiO_x films. The X-ray source was Al Kα (1486.6eV). The UV-vis transmittance and absorption spectra of NiO_x films were recorded using a Shimadzu UV-3600 UV-vis-NIR spectrophotometer. Note that all NiO_x films for UV-vis recording were deposited on the quartz substrate.

2.3 Results and discussion

Firstly, we examined the spin coating of the perovskite precursor solution on the NiO_x film without the O_2 plasma treatment. After spinning the substrate, the solution was shed rapidly owing to the hydrophobic surface of the NiO_x film. The surface of the NiO_x films was then hydrophilized by O_2 plasma treatment which made it possible to form perovskite layers on it by spin coating.

In the case of the O_2 plasma treatment under normal conditions (RF power: 18 W/15 min), which is standard for ITO surface cleaning in our laboratory, the color of the NiO_x film slightly varied from transparence to blackish transparence. *J-V* characteristics of the device showed a low fill factor (FF) of 0.17, resulting in a low PCE of 1.4% [Figure 2-2(a)]. We consider that this is probably due to damage to the NiO_x surface caused by the O_2 plasma treatment.

We then examined various O_2 plasma treatments under weaker conditions. First, the RF power and time of plasma treatment were reduced to 6.8 W and 5 min, respectively. After the treatment under those conditions, the formation of a perovskite layer on the NiO_x film was possible. The fabricated device showed an increase in FF to 0.50. Next, we examined the treatment time dependence of wettability at an RF power of 6.8 W. When the treatment time was changed from 1 to 5 min, wettability was unchanged. Thus, we fabricated the device under the weaker and shorter plasma treatment conditions to avoid damage to the NiO_x surface.

In the case of the O_2 plasma treatment under weak conditions (RF power: 6.8 W/1 min), there was no color change in the NiO_x film. Figure 2-2(b) shows the *J-V* characteristics of the device. The PSC exhibited an open circuit voltage (V_{oc}) of 1.02 V, a short-circuit current density (J_{sc}) of 19.2 mA/cm^2, a FF of 0.60, and a PCE of 11.8%. In particular, the FF markedly improved with the change in the weaker O_2 plasma treatment condition. After continuous light irradiation on the device for 10 min, the *J-V* curve slightly changed and the V_{oc}, J_{sc}, and FF values were 1.02 V, 19.0 mA/cm^2, and 0.63, respectively, yielding a PCE of 12.3%. The solar cell parameters are summarized in Table 2-1. These results indicate that NiO_x films are more sensitive to the duration and RF power of the O_2 plasma treatment than the ITO surface cleaning, and that the stronger treatment condition negatively affects the electronic states of NiO_x as HTLs for PSCs.

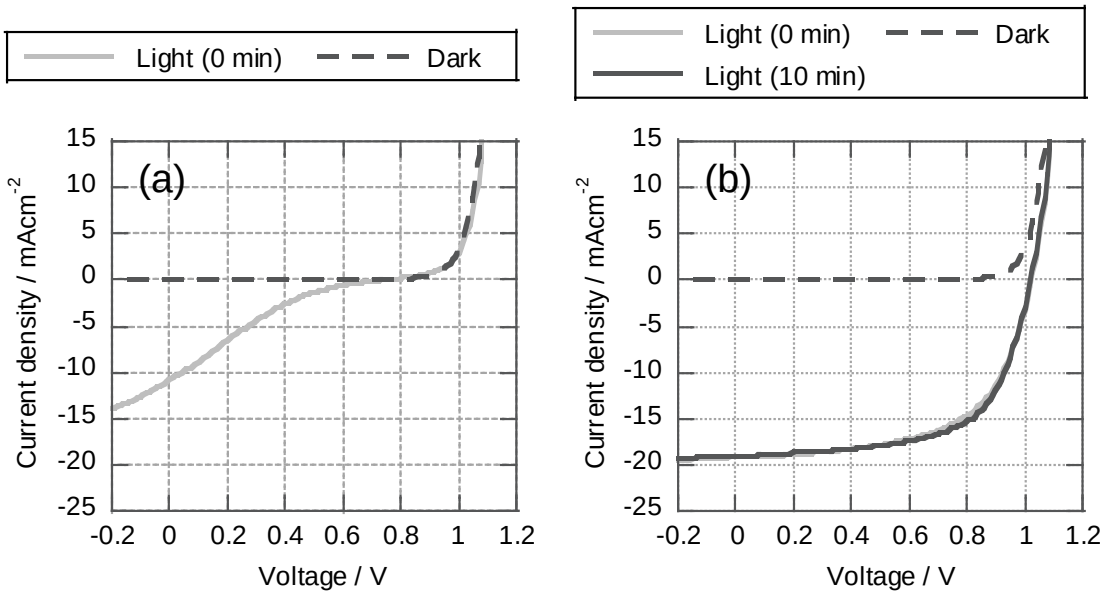

Figure 2-2. *J-V* characteristics of the device with O_2 plasma treatment under (a) normal conditions (RF power: 18 W / 15 min) and (b) weak conditions (RF power: 6.8 W / 1 min). The curves were measured in the reverse scan mode.

Table 2-1. Solar cell parameters of the devices with O_2 plasma treatment under normal and weak conditions.

		J_{sc} (mA/cm^2)	V_{oc} (V)	FF	PCE (%)
Normal conditions	average	9.2 ± 2.0	0.66 ± 0.12	0.18 ± 0.03	1.1 ± 0.3
(18 W/15 min)	best	10.8	0.73	0.17	1.4
Weak conditions	average	18.2 ± 0.8	1.02 ± 0.03	0.61 ± 0.02	11.2 ± 1.1
(6.8 W/1 min)	best	19.0	1.02	0.63	12.3

To further investigate the influence of the O_2 plasma treatment on the device performance, we measured the surface and optical properties of the NiO_x films. Figure 3 shows the contact angles of water droplets on the NiO_x films. Without the O_2 plasma treatment, the water contact angles on the NiO_x films reached 79°, which is too high for the spin coating of perovskite precursor solution. In contrast, the water contact angles on the NiO_x films with the treatment under the normal and weak conditions reached around 15°. Figure 4 shows AFM images of NiO_x surfaces without and with the O_2 plasma treatment. The surface roughness Ra was about 1.3 to 1.5 nm under all conditions. These results indicate that the NiO_x surfaces were relatively smooth and that there was no difference between the NiO_x surface roughness obtained without and with the treatment. From the contact angles and the results of AFM measurements, the improvement in wettability is probably due not to a change in surface roughness but to the addition of hydroxyl groups on the NiO_x surface

by the O_2 plasma treatment. Because there was no difference between the water contact angles obtained under the normal (RF power: 18 W/15 min) and weak (RF power: 6.8W/1 min) conditions, it is implied that the addition of hydroxyl groups on the NiO_x surface proceeded sufficiently even under the weak conditions.

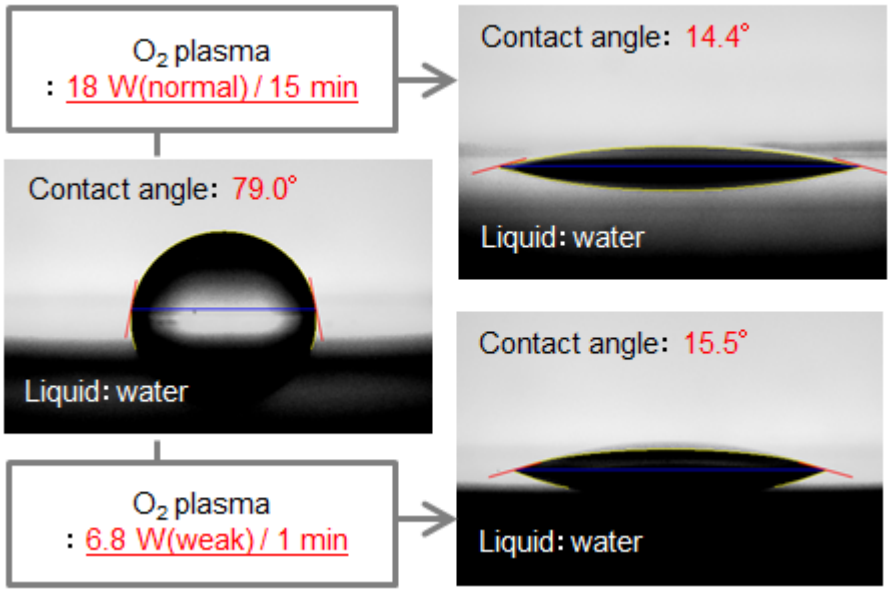

Figure 2-3. Contact angles on NiO_x surfaces without and with O_2 plasma treatment.

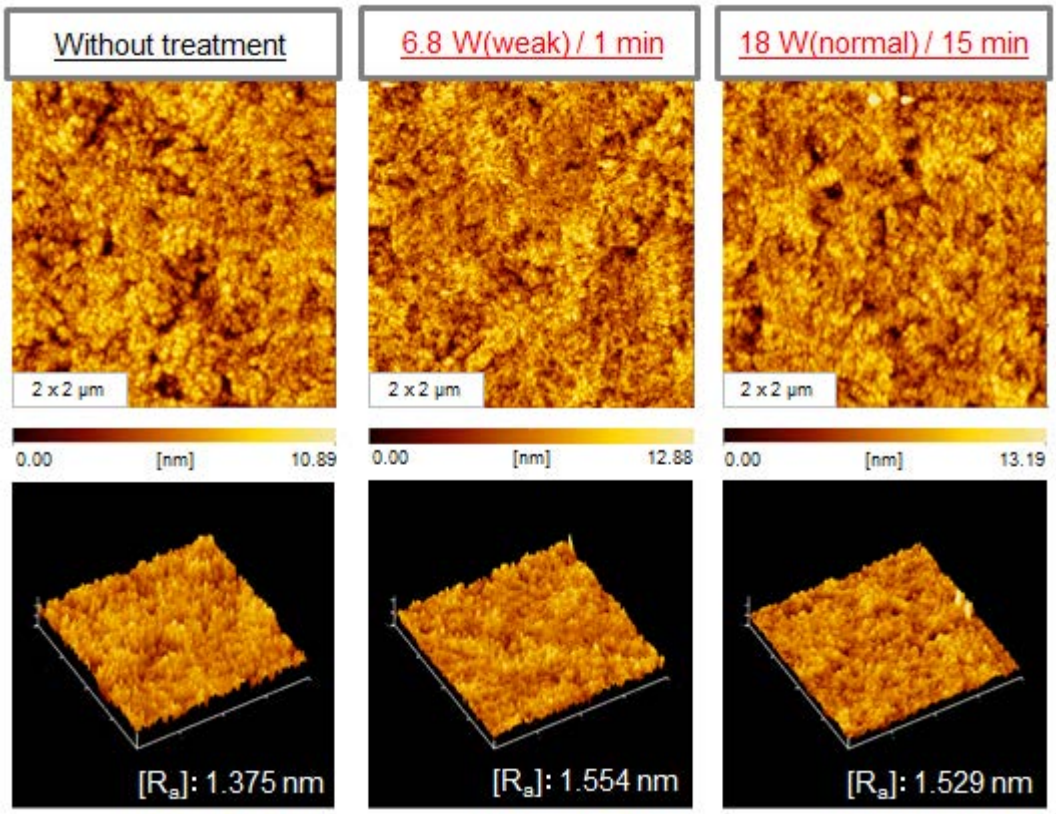

Figure 2-4. AFM images of NiO_x surfaces without and with O_2 plasma treatment.

To estimate the IP levels of NiO_x films without and with the O_2 plasma treatment, we measured PYS as shown in Figure 2-5. Without the O_2 plasma treatment, IP was 5.45 eV. In contrast, with the O_2 plasma treatment, IP was about 5.6 eV. After the O_2 plasma treatment, the valence band level was deeper by about 0.15 eV. However, there was no difference between the valence band levels obtained under the normal and weak treatment conditions.

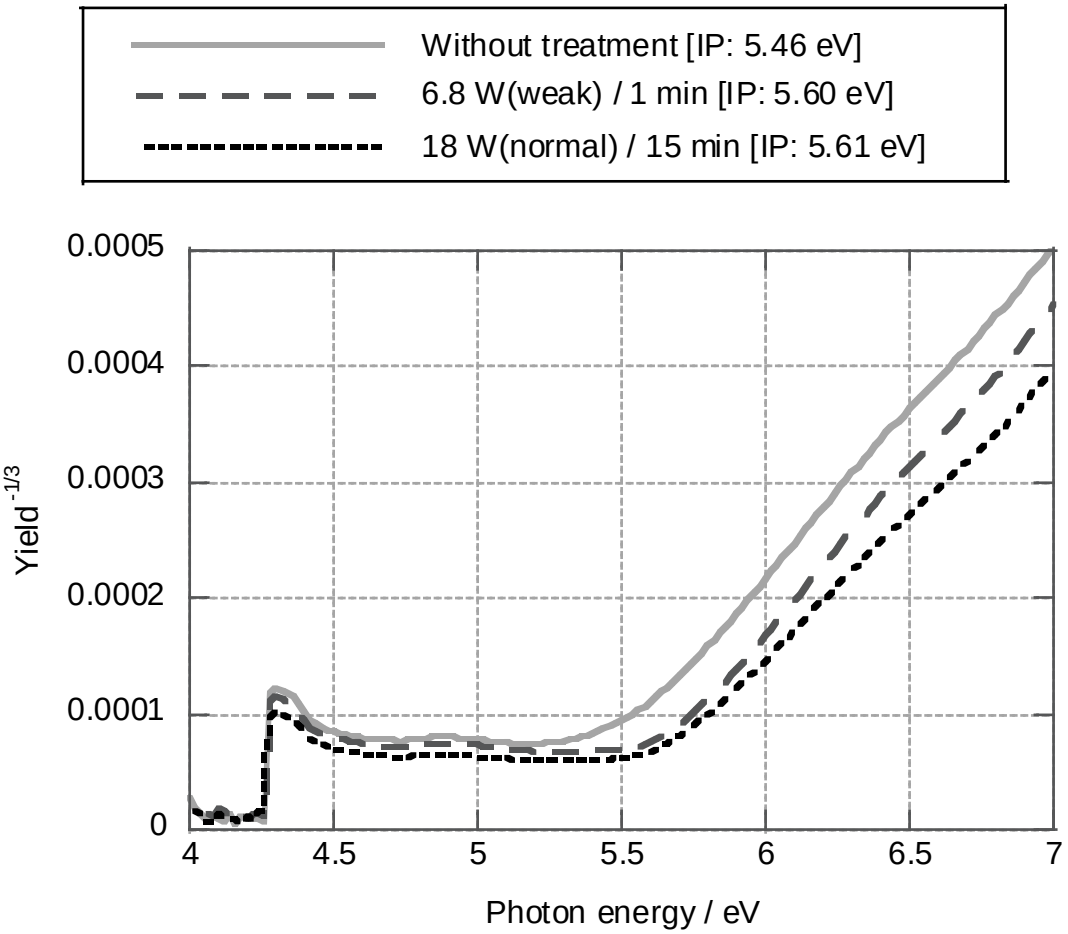

Figure 2-5. Ionization potentials of NiO_x films measured by PYS.

Figure 2-6 shows the XPS spectra of NiO_x films without and with the O_2 plasma treatment. The peak at 854 eV indicates the Ni^{2+} ion, and the peak at 856 eV indicates the Ni^{3+} ion. [13), 19)] Under the weak O_2 plasma treatment conditions, the ratio of the Ni^{2+} peak to the Ni^{3+} peak was almost unchanged from those without the treatment. On the other hand, under the normal conditions, the Ni^{2+} peak intensity markedly decreased. The water contact angle, AFM, and PYS were used to observe the NiO_x surface properties. In contrast, XPS was used for the bulk NiO_x film because it was very thin (10 nm). From these results, it can be presumed that the composition of the bulk NiO_x film approaches Ni_2O_3. Generally, NiO_x is composed of Ni^{2+}, Ni^{3+}, and the vacancy in the unit cell, and the hopping of electrons from Ni^{2+} to Ni^{3+} is the driving force of the electron conductivity in NiO_x. The decrease in the Ni^{2+} component as a result of the O_2 plasma treatment under the normal conditions may change the electrical and optical properties of NiO_x films.

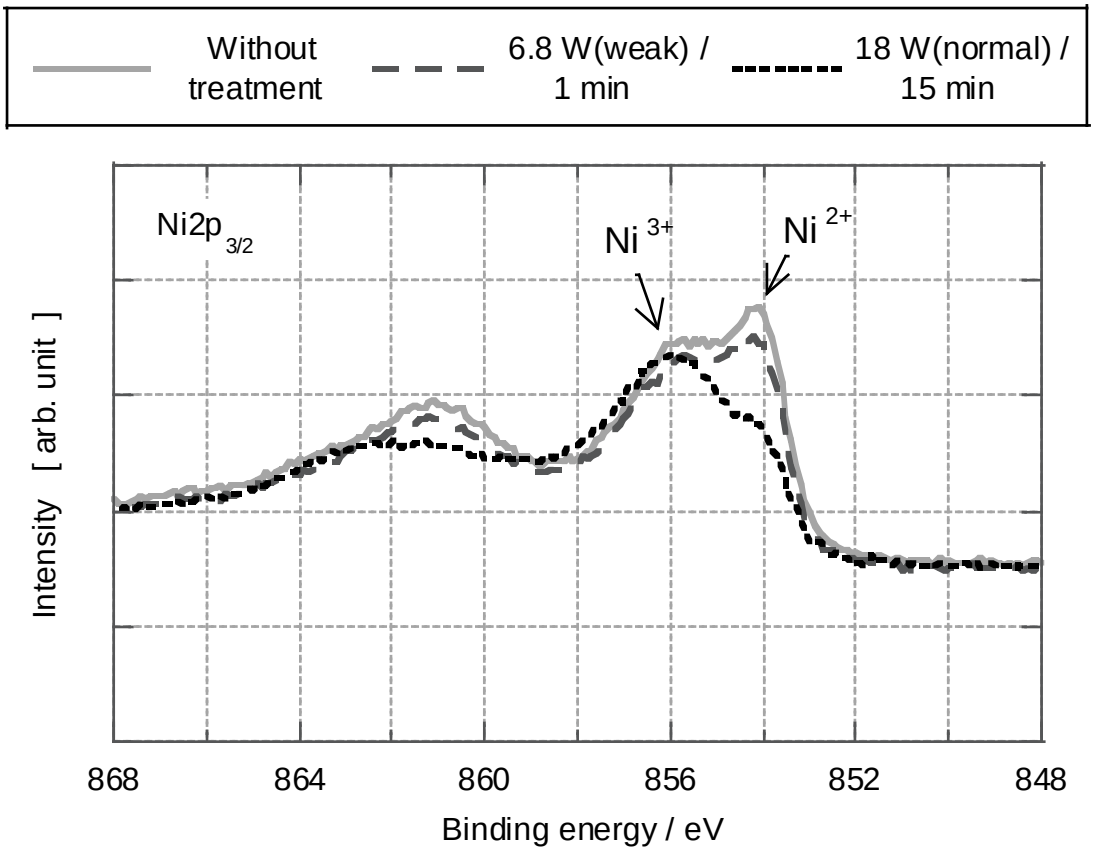

Figure 2-6. XPS spectra of NiO_x films without and with O_2 plasma treatment.

Figure 2-7 shows the transmittance spectra of NiO_x films. After the weak treatment, transmittance decreases by only 1% compared with that of films without the treatment in the range from 300 to 1000 nm. In contrast, after the normal treatment, transmittance decreases by 4% in the same range. In addition, the color of the NiO_x film slightly varied from transparence to blackish transparence. This result indicates that NiO_x film oxidization occurred under the normal O_2 plasma treatment and that the Ni^{3+}/Ni^{2+} ratio in the bulk NiO_x film increased. This phenomenon is consistent with the previous reports. [19), 22)]

Figure 2-8 shows the absorption spectra converted from the transmittance spectra. Band-gap energies were calculated from the onset of the absorption spectra. As a result, in the case without the treatment, the band gap energy was 3.53 eV. This value is similar to the reported data [1)]. Additionally, there was no large difference in band-gap energy between the films without and with the weak treatment. However, in the case of the normal treatment, the band-gap energy was larger by about 0.1 eV and the absorbance increased over a wide range from 1.2 to 3.5 eV.

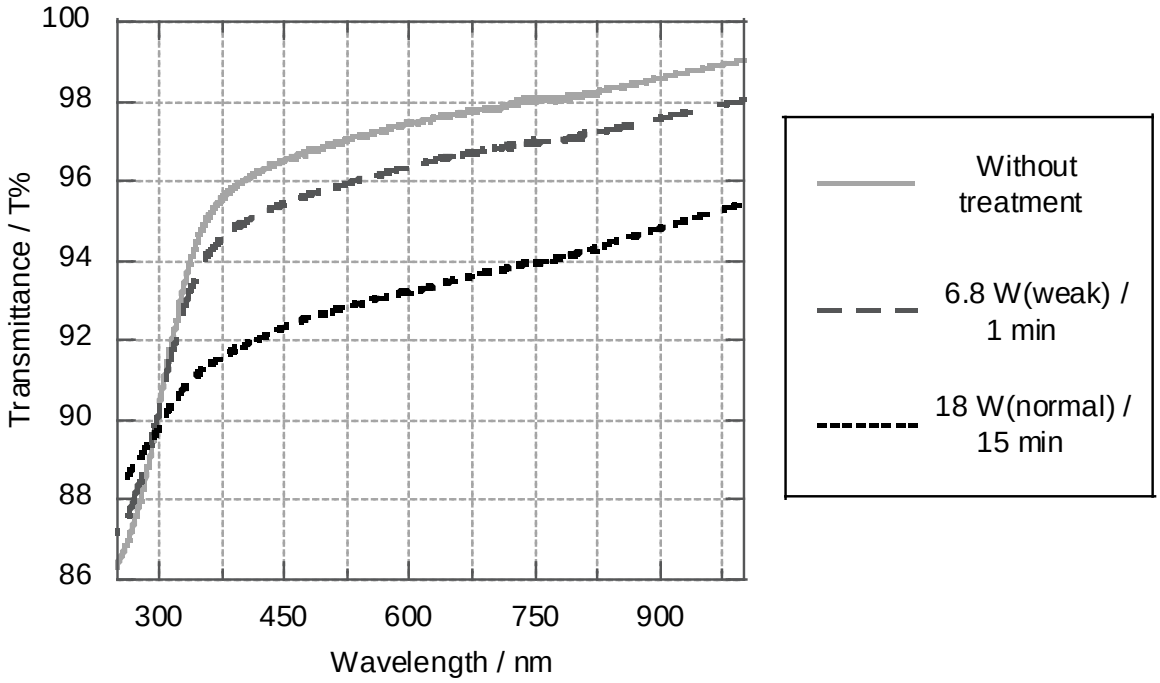

Figure 2-7. Transmittance spectra of NiO_x films

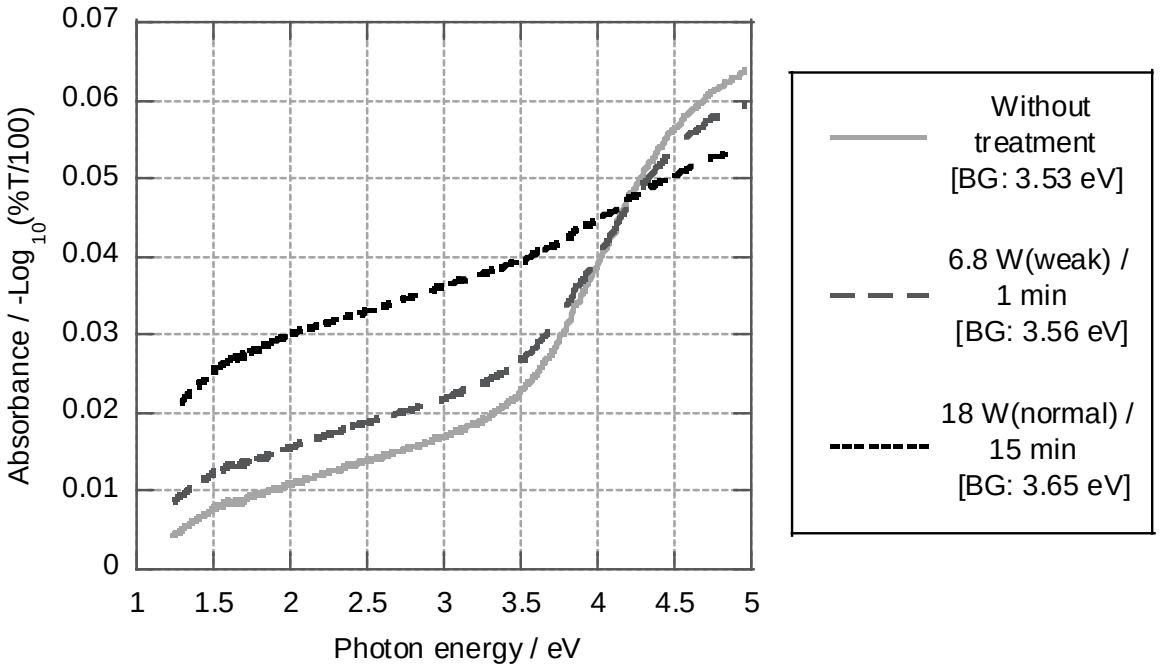

Figure 2-8. Absorption spectra converted from the transmittance spectra.

Islam *et al*. reported PSCs with sputter-deposited NiO_x films and the transmission spectra of NiO_x films (thicknesses of 60-70 nm) at different Argon sputtering pressures (0.5-6.5 Pa). [19] The NiO_x film prepared at 0.5 Pa, which showed the highest Ni^{3+} / Ni^{2+} ratio among the prepared films, was blackish and had a low transmittance of 60% at 550 nm, whereas our

prepared NiO_x films (thickness of 10 nm) with the normal treatment had a high transmittance of 93% at 550 nm (Figure 2-7). They reported that the device with the NiO_x film prepared at 0.5 Pa showed low performance owing to the optical loss of the blackish NiO_x film. In contrast, since our prepared NiO_x films with the normal treatment did not have such a low transmittance, optical loss appears to be relatively low. We therefore suggest that in-gap states were formed by the normal treatment. From our experimental data on NiO_x films, we produced a band diagram (Figure 2-9). After the normal treatment, the low device performance was possibly caused by the in-gap states, which act as recombination sites. Park *et al*. examined vacancy defects in NiO by first-principles calculations.[23] They reported that the defect states associated with nickel or oxygen vacancies are identified within the energy gap. However, there is no experimental report concerning the in-gap states of NiO_x. More detailed experiments on NiO_x films will be needed in the future.

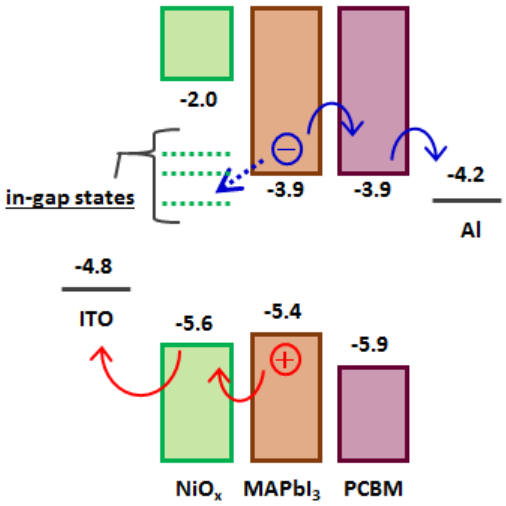

Figure 2-9. Band diagram.

2.4 Conclusions

We investigated the influence of O_2 plasma treatment on the NiO_x layer in PSCs. The treatment made it possible to form the perovskite layer on the NiO_x layer by spin coating. We found that NiO_x films are sensitive to O_2 plasma treatment and that a stronger treatment negatively affects the electronic states of NiO_x as HTLs for PSCs. The maximum PCE of the device under the optimized O_2 plasma condition reached 12.3%.

References

1) L. Meng, J. You, T. F. Guo, and Y. Yang, *Acc. Chem. Rec.* **49**, 155 (2016).
2) W. Yan, S. Ye, Y. Li, W. Sun, H. Rao, Z. Liu, Z. Bian, and C. Huang, *Adv. Energy Mater.* **6**, 1600474 (2016).
3) J. Y. Jeng, Y. F. Chiang, M. H. Lee, S. R. Peng, T. F. Guo, P. Chen, and T. C. Wen, *Adv. Mater.* **25**, 3727 (2013).
4) C. C. Wu, C. H. Ching, Z. L. Tseng, M. K. Nazeeruddin, A. Hagfeldt, and M. Grätzel, *Energy Environ. Sci.* **8**, 2725 (2015).
5) S. Yu, W. Sun, Y. Li, W. Yan, H. Peng, Z Bian, Z Liu, and C Huang, *Nano Lett.* **15**, 3723 (2015).
6) W. Y. Chen, L. L. Deng, S. M. Dai, X. Wang, C. B. Tian, X. X. Zhan, S. Y. Xie, R. B. Huang, and L. S. Zheng, *J. Mater. Chem. A* **3**, 19353 (2015).
7) C. Zuo and L. Ding, *Small* **11**, 5528 (2015).
8) J. W. Jung, C. C. Chueh, and A. K. Y. Jen, *Adv. Mater.* **27**, 7874 (2015).
9) W. Chen, Y. Wu, Y. Yue, J. Liu, W. Zhang, X. Yang, H. Chen, E. Bi, I. Ashraful, M. Grätzel, and L. Han, *Science* **350**, 944 (2015).
10) J. You, L. Meng, T. B. Song, T. F. Guo, Y. M. Yang, W. H. Chang, Z. Hong, H. Chen, H. Zhou, Q. Chen, Y. Liu, N. D. Marco, and Y. Yang, *Nat. Nanotechnol.* **11**, 75 (2016).
11) P. Docampo, J. M. Ball, M. Darwich, G. E. Eperon, and H. J. Snaith, *Nat. Commun.* **4**, 2761 (2013).
12) H. Zhang, J. Cheng, F. Lin, H. He, J. Mao, K. S. Wong, A. K. Y. Jen, and W. C. H. Choy, *ACS Nano* **10**, 1503 (2016).
13) X. Yin, M. Que, Y. Xing, and W. Que. *J. Mater. Chem. A* **3**, 24495 (2015).
14) Y. Wu, F. Xie, H. Chen, X. Yang, H. Su, M. Cai, Z. Zhou, T. Noda, and L. Han, *Adv. Mater.* **29**, 1701073 (2017).
15) I. J. Park, G. Kang, M. A. Park, J. S. Kim, S. W. Seo, D. H. Kim, K. Zhu, T. Park, and J. Y. Kim, *ChemSusChem* **10**, 2660 (2017).
16) J. H. Park, J. Seo, S. Park, S. S. Shin, Y. C. Kim, N. J. Jeon, H.-W. Shin, T. K. Ahn, J. H. Noh, S. C. Yoon, C. S. Hwang, and S. I. Seok, *Adv. Mater.* **27**, 4013 (2015).
17) Z. Qiu, H. Gang, G. Zheng, S. Yuan, H. Zhang, X. Zhu, H. Zhou, and B. Cao, *J. Mater. Chem. C* **5**, 7084 (2017).
18) T. Miyadera, T. Sugita, H. Tampo, K. Matsubara, and M. Chikamatsu, *ACS Appl. Mater. Interfaces* **8**, 26013 (2016).
19) M. B. Islam, M. Yanagida, Y. Shirai, Y. Nabetani, and K. Miyano, *ACS Omega* **2**, 2291

(2017).

20) Y. Nishihara, M. Chikamatsu, S. Kazaoui, T. Miyadera, Y. Yoshida, *Ext. Abstr. Solid State Devices and Materials*, 2017, p. 109.

21) N. Ahn, D. Y. Son, I. H. Jang, S. M. Kang, M. Choi, and N. G. Park, *J. Am. Chem. Soc.* **137**, 8696 (2015).

22) A. R. West, *Solid State Chemistry and Its Applications* (Wiley, New York, 2014) 2nd ed., Chap. 8.

23) S. Park, H. S. Ahn, C. K. Lee, H. Kim, H. Jin, H. S. Lee, S. Seo, J. Yu, and S. Han, *Phys. Rev. B* **77,** 134103 (2008)

Chapter III

Influence of p-type Doping on Perovskite Solar Cells Fabricated with Dithiophene-Benzene Copolymer as the Hole Transporting Layer

3.1 Introduction

Hole-transporting layers (HTLs) determine the performance of PSCs. Therefore, the study of hole-transporting materials (HTMs) is active and focuses on the following three characteristics: long-term stability during exposure to air, hole mobility to deliver holes to the backside of the electrode, and frontier energy levels that match those of perovskite layers.

2,2',7,7'-tetrakis(*N*,*N*-di-*p*-methoxyphenylamine)-9,9'-spirobifluorene (Spiro-OMeTAD) is widely employed as an HTM of PSCs. Typically, lithium bis(trifluoromethanesulfonyl) imide (Li-TFSI) is added as a dopant due to the low charge mobility of spiro-OMeTAD. However, the hygroscopic feature of the lithium salts will degrade PSCs during operation. In addition, spiro-OMeTAD is expensive because the synthesis process has been complicated. For these reasons, alternative materials have been explored. The exploration of dopant-free HTM has been tried widely in both small molecules[1-13] and conjugated polymers.[14-28] For example, a kind of metal-porphyrin complex[1] is reported as small molecule HTMs. Including this complex, many small molecule materials incorporating triphenylamine groups into the molecular structure have been synthesized.[2-5] In conjugated polymer HTMs, frontier energy levels are tried to control via engineering the side-chain[15,16,22,29] and substituting atoms in the aromatic rings.[17] As a results, the compatibility of band alignment and the stability are improved. Non-hygroscopic p-type dopants have been explored from another viewpoint. Tris(pentafluorophenyl)borane (BCF), an organic Lewis acid, has been employed as dopant to HTM.[29-32]

The copolymer dithiophene-benzene (DTB) is reported to have a high stability and a higher short circuit current density (J_{sc}) than other polymer semiconductors.[33] In addition, DTB may be relatively inexpensive because the synthesis procedure is not complicated. However, the effects of oxygen and dopant on DTB have yet to be examined in detail. Therefore, we focused on investigating the effects of p-type doping on DTB as an HTL in PSCs.

In this study, DTB copolymers were prepared by two different copolymerization methods to obtain high and low molecular weight DTB. In addition, BCF was selected as a non-hygroscopic p-type dopant. We fabricated mesoporous-type PSC devices employing each DTB copolymer as an HTM under nitrogen. We then verified the influence of oxygen-doping by keeping DTB copolymers in dry air and measuring the doping effect on BCF.[34] In addition, we focused on the cohesiveness of each DTB copolymer and proposed an oxygen-doping mechanism in DTB films.

3.2. Experimental section

The mesoporous-type PSC devices with a layered structure of fluorine-doping tin oxide (FTO) / compact-TiO_2 (c-TiO_2) / mesoporous-TiO_2 (m-TiO_2) / perovskite / HTL / Au is shown in Figure 1(a). FTO substrates were purchased from Nippon Sheet Glass (sheet resistance ≤ 10 Ω/sq). First, c-TiO_2 layers were formed on the FTO layer by spray pyrolysis. Titanium diisopropoxide bis(acetylacetonate) (Aldrich, 75 wt% in isopropanol) was further diluted with ethanol at 6 vol%. The diluted solution was sprayed at 400 °C and heated at 500 °C for 10 min. Next, m-TiO_2 layers were formed by spin coating a TiO_2 paste (Dyesol 18NRT) diluted with ethanol (14 wt%) at 2000 rpm for 30 s, which was then calcined at 120 °C for 15 min and 450 °C for 0.5 h. Perovskite layers were formed by anti-solvent method in a nitrogen-filled glove box. A precursor solution of CsI (42 μL of a 1.5 M stock solution in dimethyl sulfoxide (DMSO)), formamidine hydroiodide (FAI, 172 mg), methylamine hydrobromide (MABr, 22.4 mg), PbI_2 (507 mg), and $PbBr_2$ (73.4 mg) in 1 mL of a 4:1 volume ratio of *N*,*N*-Dimethylformamide (DMF) and DMSO was adjusted the composition $Cs_{0.05}FA_{0.79}MA_{0.16}PbI_{2.52}Br_{0.48}$. Perovskite films were deposited onto m-TiO_2 layers using a two-step spin-coating procedure. The first step was 1000 rpm for 10 s, and the second step was 6000 rpm for 20 s. To form smooth perovskite films, chlorobenzene (approximately 200 μL) was dropped onto the film during the second step at 15 s of the 20 s spin. The as-prepared films were heated at 40 °C for at least 5 min, 60 °C for 5 min, 70 °C for 5 min, and 100 °C for 1 h. We synthesized DTB copolymers as shown in Figure 1(b). High molecular weight DTB was synthesized with the Stille coupling reaction,[33] and low molecular weight DTB was synthesized with a slight modification of the Suzuki coupling reaction.[35] Gel permeation chromatography (GPC) analysis was performed with a Shimadzu HIC-6A chromatography system using tetrahydrofuran as the eluent and polystyrene standards. For high and low molecular weight DTB films, the weight-average molecular weights (M_w) were 1.55×10^4 and 4.52×10^3, and the polydispersity indexes were 1.33 and 1.03, respectively. HTLs were fabricated in a nitrogen-filled glove box. In the case of DTB devices, HTLs were deposited by spin coating of the dissolved DTB in chlorobenzene (7.5 mg mL^{-1}). BCF (Figure 1(c)) was added to the DTB solution as needed. Substrates and DTB solution were preheated at 80 °C on a hot plate. Finally, Au electrodes were formed by thermal evaporation under vacuum at 5.0×10^{-4} Pa. Figure 1(d) is cross section scanning electron microscope (SEM) image of high molecular weight DTB-based device with BCF (4.0 wt%) doping. The measured film thickness of each layer is as follows: FTO (710 nm) / TiO_2 (180 nm) / Perovskite (550 nm) / DTB (30 nm) / Au (50 nm). In this device, the film

thickness of DTB layer less than 50 nm. This value is sufficiently thin as HTL.

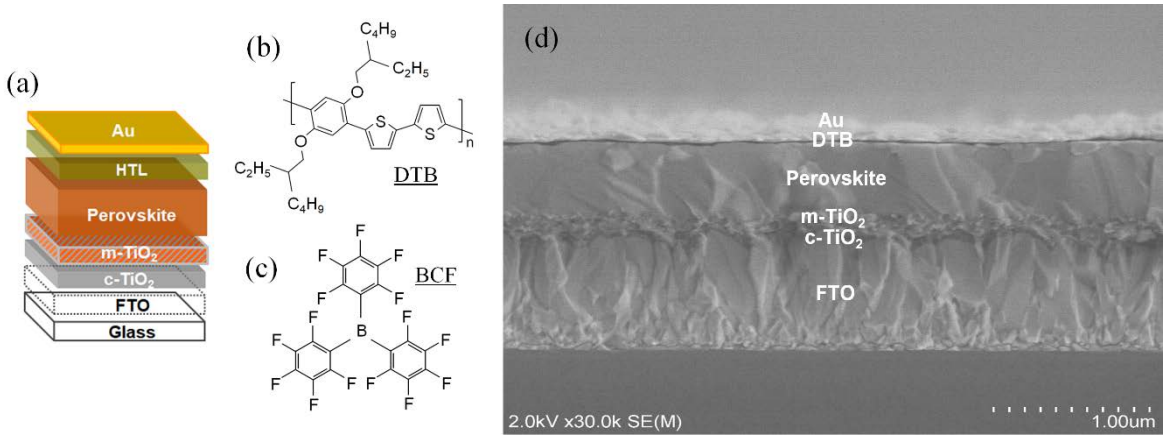

Figure 3-1. Structure of PSC devices (a), molecular structure of DTB (b) and BCF (c), and cross-section SEM image of the high molecular weight DTB device with BCF-doping.

J–V measurements of the devices under AM1.5G solar simulator illumination (Wacom WXS-80C-3 with a 300 W Xe lamp and an AM 1.5 filter) were performed with a DC voltage/current source monitor (Advantest R6243) in air at room temperature without encapsulation. For all measurements, devices were equipped with a 0.119 cm^2 metal aperture to define the active area. Device samples were kept in a desiccator in which humidity was controlled at < 5% relative humidity. During measurement procedures, samples were exposed to room air.

The surface morphology of DTB films on glass substrates was observed by atomic force microscopy (AFM, SII NanoTechnology Nanonavi/E-sweep) in the dynamic mode. The ultraviolet-visible (UV-Vis) absorption spectra of DTB films on quartz substrates were recorded using a Shimadzu UV-3600 UV-vis-NIR spectrophotometer.

3.3 Results and discussion

Firstly, we fabricated PSC devices using high and low molecular weight DTB copolymers without dopant, and then examined the time dependence of device performance. Typical *J–V* curves obtained after PSC devices were exposed to air for 5 h are shown in Figure 2(a). In the case of high molecular weight DTB-based devices, the PCE is 3.05%, with a low fill factor (FF) value of 0.25, and a series resistance (Rs) of 48.04 Ω cm^2. In the case of low molecular weight DTB-based devices, the PCE is higher (10.0%), with an FF value of 0.52, and an Rs of 7.28 Ω cm^2. Typical *J–V* curves obtained after the devices were maintained in dry air for 173 h are shown in Figure 2(b). In the case of high molecular weight

DTB-based devices, the PCE improves to 16.20%, with the FF value rising to 0.73. On the other hand, in the case of low molecular weight DTB-based devices, the PCE improves to 14.66%, with the FF rising to 0.67; these values are lower than those seen in of high molecular weight DTB-based devices (Table 3-1).

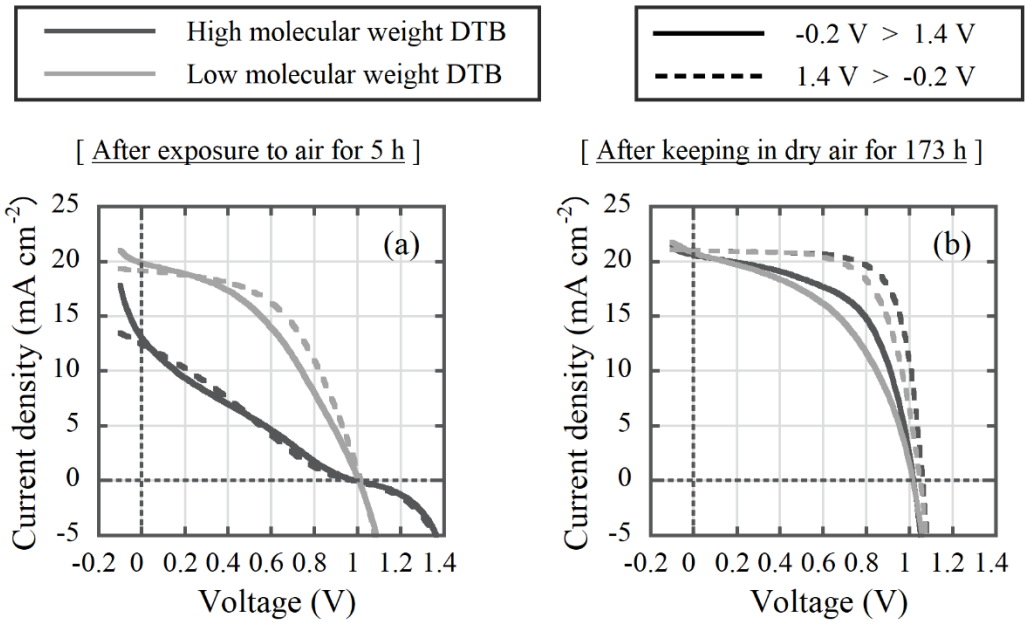

Figure 3-2. Typical *J–V* curves of high and low molecular weight DTB devices after exposure to air for 5 h (a) and after keeping in dry air for 173 h (b).

The time dependence of PCE and Rs for high and low molecular weight DTB-based devices without dopant is shown in Figure 3-3. As air exposure time increases, PCE increases, and Rs decreases. These results imply that the carrier density in DTB increases due to oxygen-doping. Because the HTLs were fabricated under nitrogen, the oxygen-doping to DTB was probably insufficient after exposure to air for only 5 h. We then compared the *J–V* characteristics from high and low molecular weight DTB-based devices. PCE histograms and average of photovoltaic parameters are shown in Figure 3-4. Initially, the average PCE values of low and high molecular weight DTB-based devices are 9.07% and 2.41%, respectively. After oxygen-doping reached saturation, average PCE values of low and high molecular weight DTB-based devices improve to 14.09% and 15.77%, respectively. We attempted to understand the mechanism that caused this higher PCE value in high molecular weight DTB-based devices by evaluating the cohesiveness of DTB copolymers.

Table 3-1. Solar cell parameters of PSC devices fabricated with high and low molecular weight DTB. [a]Mean ± standard deviation [b]Values from typical *J-V* curves.

HTM	J_{sc} [mA cm^{-2}]	V_{oc} [V]	FF	PCE [%]	Rs [Ωcm^2]
After exposure to air for 5 h					
High molecular weight DTB	10.82 ± 1.07[(a)] (12.47)[(b)]	0.97 ± 0.02 (0.98)	0.23 ± 0.01 (0.25)	2.41 ± 0.39 (3.05)	69.68 ± 18.30 (48.04)
Low molecular weight DTB	19.35 ± 0.24 (19.18)	1.01 ± 0.02 (1.01)	0.46 ± 0.02 (0.52)	9.07 ± 0.48 (10.00)	8.87 ± 1.20 (7.28)
After keeping in dry air for 173 h					
High molecular weight DTB	20.89 ± 0.37 (21.01)	1.05 ± 0.02 (1.06)	0.72 ± 0.01 (0.73)	15.77 ± 0.31 (16.20)	3.77 ± 0.18 (3.63)
Low molecular weight DTB	20.44 ± 0.34 (20.98)	1.04 ± 0.01 (1.05)	0.66 ± 0.01 (0.67)	14.09 ± 0.47 (14.66)	4.73 ± 0.16 (4.73)

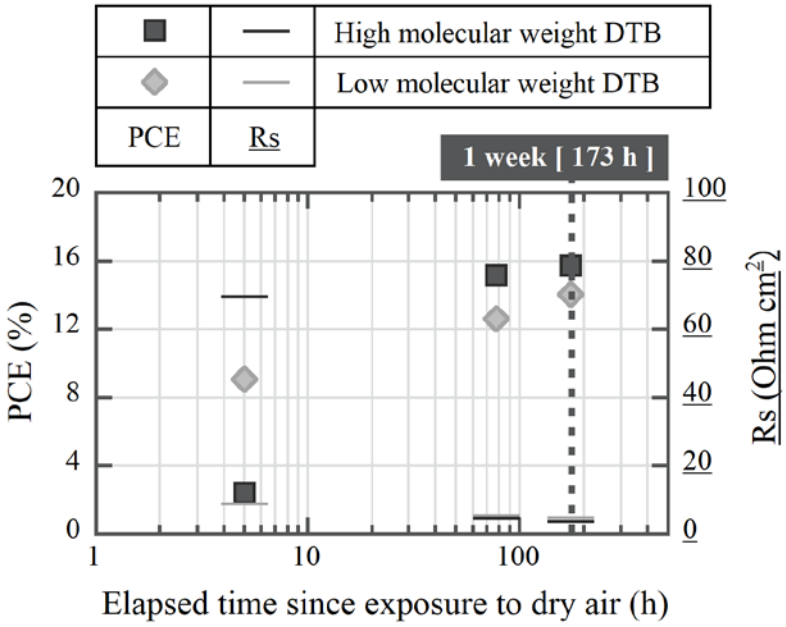

Figure 3-3. The time dependence of PCE and Rs of high and low molecular weight DTB devices without dopant.

AFM images of each DTB film are shown in Figure 3-5. In high molecular weight DTB film, grain boundaries are clearly observed. However, in low molecular weight DTB films, the morphology appears amorphous, and several holes are observed. The UV-Vis absorption spectra, normalized to the maximum value of absorbance, are shown in Figure 3-6. The main absorption peak of low molecular weight films is located at 495 nm. On the other hand, the

main absorption peak of high molecular weight films is located at 504 nm; i.e., redshifted by 9 nm. In addition, the shoulder peak of high molecular weight DTB is stronger than that of low molecular weight DTB. These results indicate that high molecular weight DTB has strong cohesion.

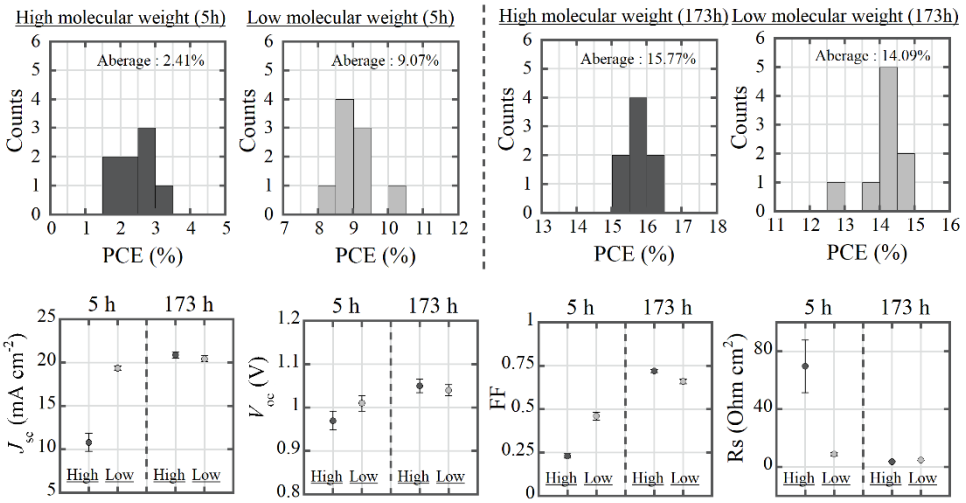

Figure 3-4. PCE histograms of high and low molecular weight DTB devices.

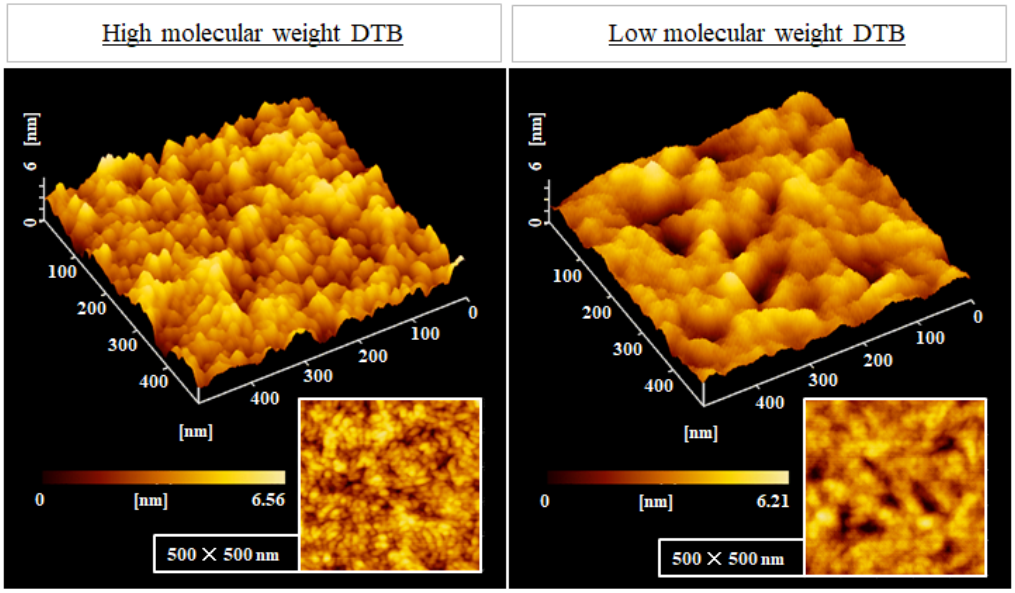

Figure 3-5. AFM images of high and low molecular weight DTB films.

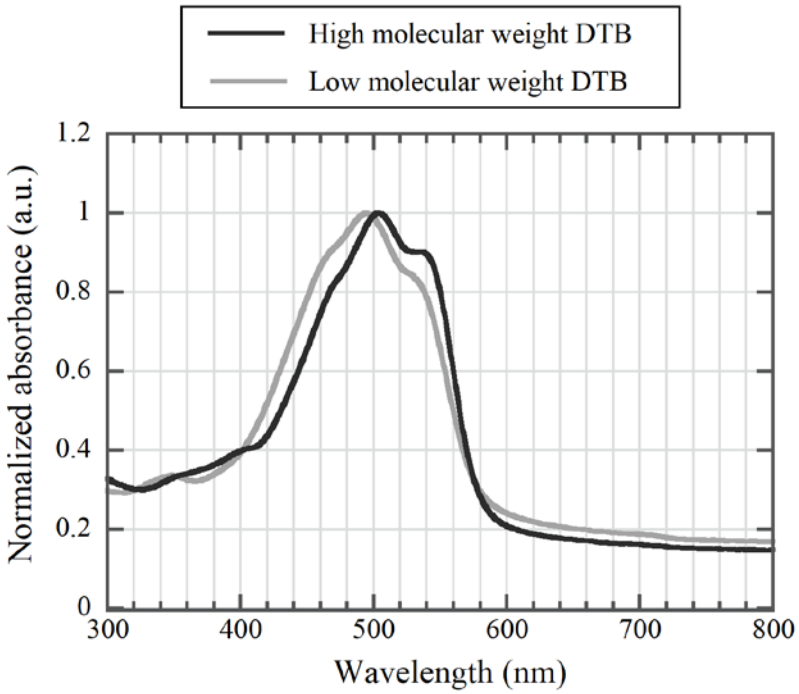

Figure 3-6. UV-Vis absorption spectra of high and low molecular weight DTB films.

Based on these observations, we propose an oxygen-doping mechanism for DTB films. In the case of high molecular weight DTB, the films are compact, with strong cohesion. Therefore, as shown in Figure 3-7 (a), oxygen diffuses very slowly into these films. Also, its takes longer time for oxygen to reach the inside of each grain because of its strong cohesiveness. On the other hand, in the case of low molecular weight DTB, the films are amorphous, with pinholes. Therefore, as shown in Figure 3-7 (b), oxygen diffuses quickly into these films. Also, oxygen easily reaches inside of each grain because of its amorphous structure. Initially, the PCE of low molecular weight DTB-based devices is superior to that of high molecular weight DTB-based devices because of the quickly oxygen-doping. After oxygen-doping is saturated, the superior molecular order of the high molecular weight DTB film in the fabricated devices yields a higher PCE value than low molecular weight DTB-based devices.

Secondly, we investigated the impact of BCF as a p-type dopant on PSC devices fabricated with high molecular weight DTB copolymer. Typical *J–V* characteristics after exposure to air for 5 h are shown in Figure 3-8(a). In the case of devices without BCF, the initial PCE value is 2.07%, with an FF of 0.24, and Rs is 48.43 Ω cm^2. On the other hand, when BCF (4.0 wt%) was added to DTB, the initial PCE improves to 12.12%, the FF rises to 0.55, and Rs decreases to 10.83 Ω cm^2. When BCF (8.0 wt%) was added to DTB, the initial PCE further improves to 14.84%, the FF rises to 0.69, and Rs decreases to 4.99 Ω cm^2

without maintaining the device for a long time in dry air. Typical *J–V* characteristics oxygen-doping is saturated by keeping the devices in dry air for 77 h are shown in Figure 3-8(b). In the case of devices without BCF, the PCE value is 16.30%, the FF is 0.72, and Rs is 3.99 Ω cm^2. When BCF (4.0 wt%) was added to DTB, the PCE value is 16.89%, the FF is 0.73, and Rs is 3.75 Ω cm^2; this formulation yielded the maximum PCE of DTB-based devices evaluated in this study. When BCF (8.0 wt%) was added to DTB, the PCE value is 15.98%, the FF is 0.71, and Rs is 4.04 Ω cm^2 (Table 3-2).

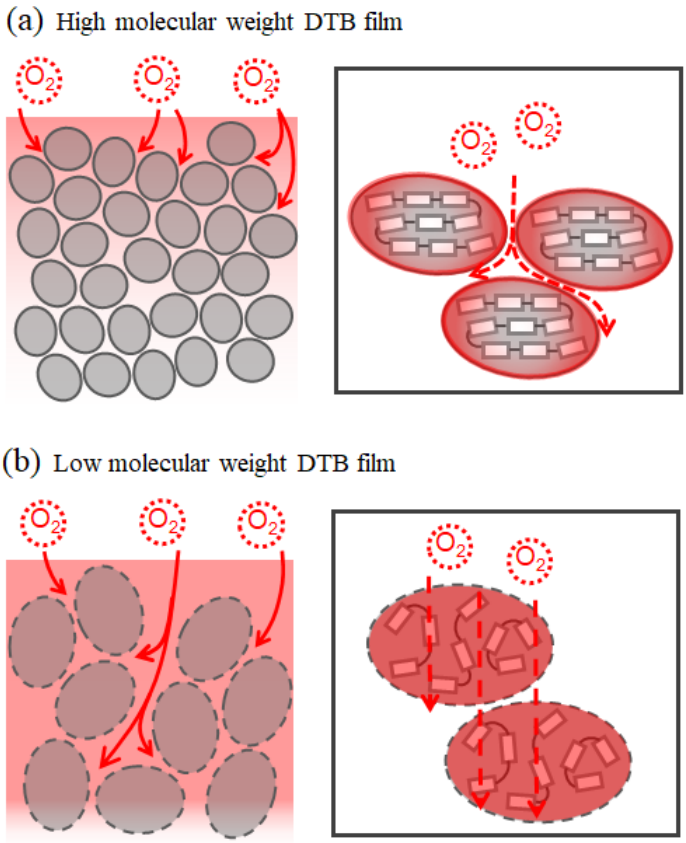

Figure 3-7. Schematic illustrations of oxygen-doping mechanism for DTB films.

The relationship of time in dry air on the performance (i.e., PCE and Rs) of high molecular weight DTB-based devices with or without BCF-doping is shown in Figure 9. And then, PCE histograms and average of photovoltaic parameters are shown in Figure 10. With BCF addition, PCE increases and Rs decreases initially. After 77 h in dry air, average PCE improves to 15%–16%, regardless of BCF concentration. After 173 h in dry air, average PCE decreases slightly. These results indicate that oxygen-doping was saturated after 77 h in dry air.

The impact of BCF content assessed by AFM of high molecular weight DTB films is shown in Figure 11. There are no remarkable differences in the AFM images at each BCF

concentration. The impact of BCF content assessed by UV-Vis absorption of high molecular weight DTB films is shown in Figure 12. Each spectrum is normalized to the maximum value of absorbance. There are no observable differences in the wavelength of the main absorption peak or the intensity of the shoulder peak at each BCF concentration. These results show that the cohesiveness of DTB films is not affected by BCF-doping. These results indicate that the increase in carrier density in DTB occurs due to BCF-doping. Doping has been explained in terms of the formation of Lewis acid-base adducts.[36] The electrophilic borane of BCF binds to a moiety carrying an accessible lone pair of electrons at the sulfur atoms of the thiophene rings. As a result, hole-doping occurs on the thiophene rings of DTB, leading to a reduction in Rs. Therefore, the PCE of devices with BCF yielded a higher PCE value than devices without BCF after exposure to air for 5 h.

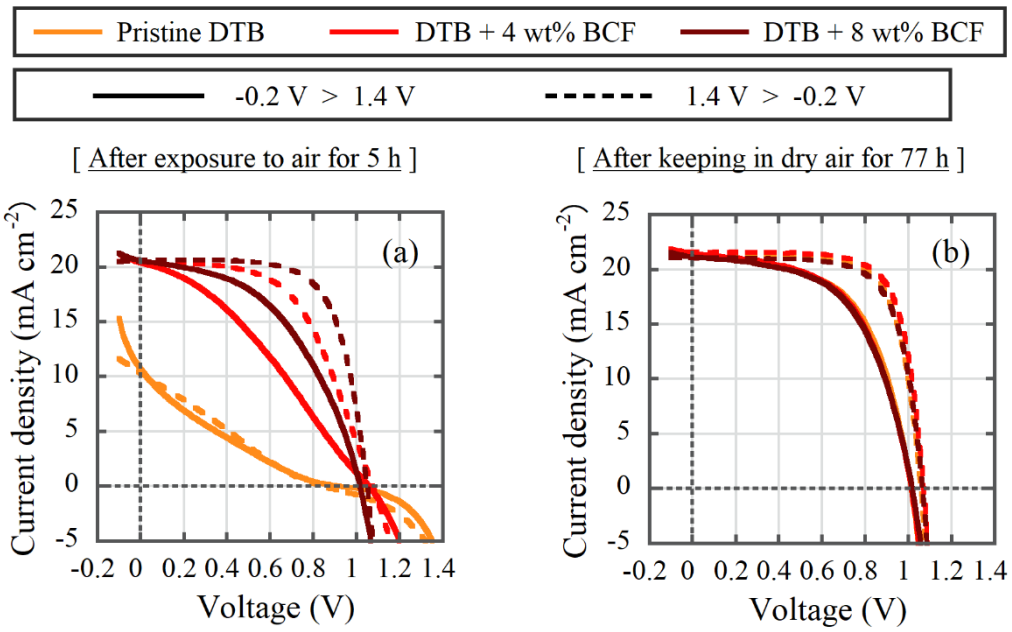

Figure 3-8. Typical *J–V* curves of high molecular weight DTB devices without and with BCF-doping at after exposure to air for 5 h (a) and at after keeping in dry air for 77 h (b).

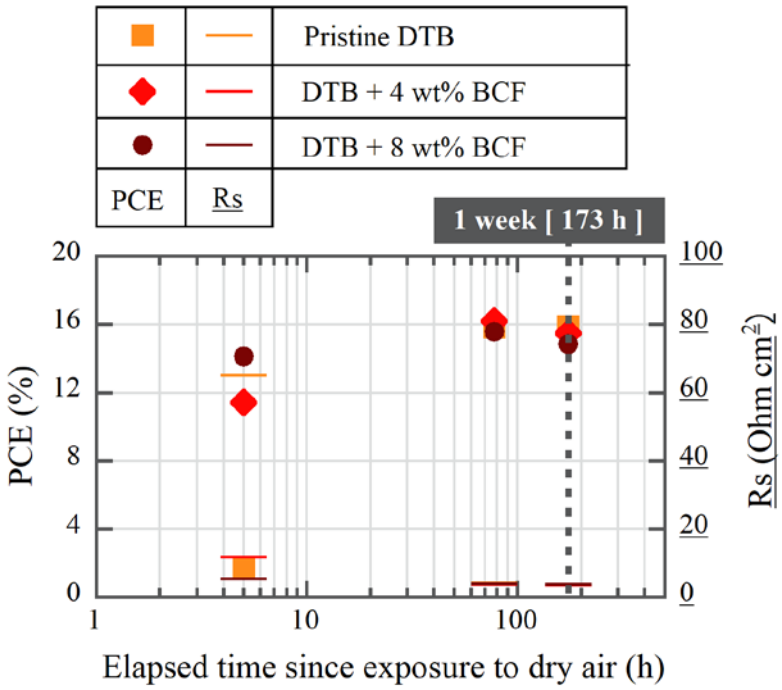

Figure 3-9. Time dependence of the PCE and Rs values of high molecular weight DTB devices without and with BCF-doping.

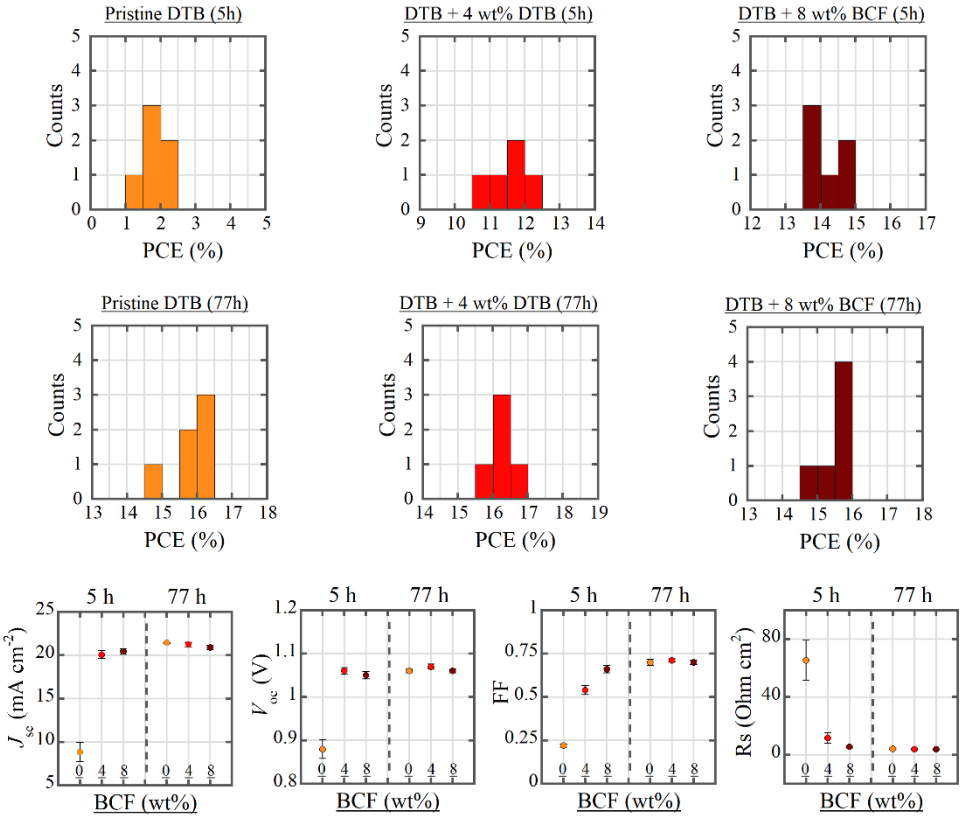

Figure 3-10. PCE histograms of high molecular weight DTB devices with and without BCF-doping.

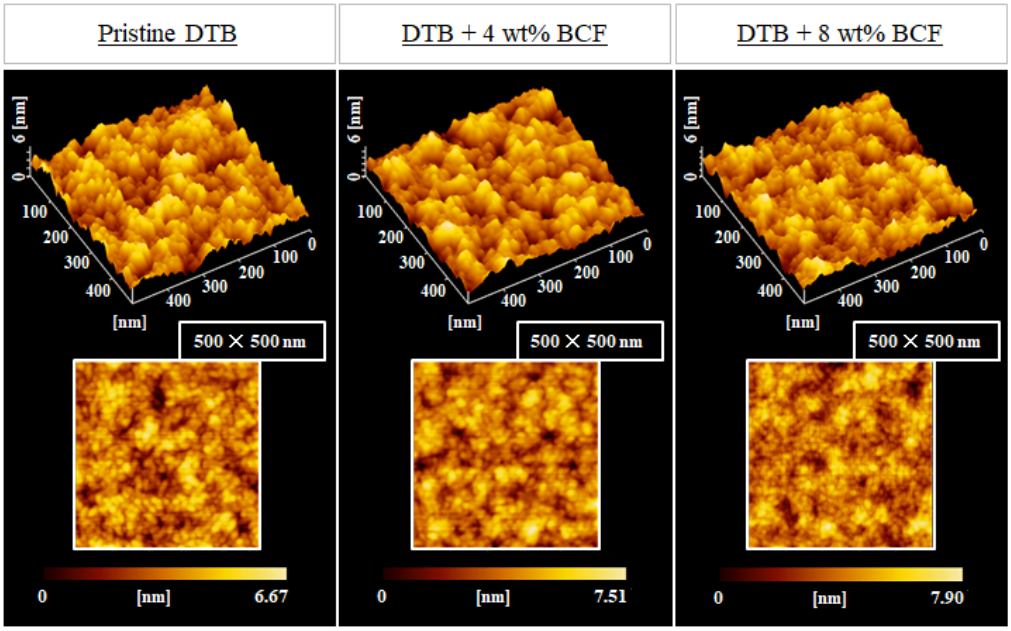

Figure 3-11. AFM images of high molecular weight DTB films without and with BCF-doping.

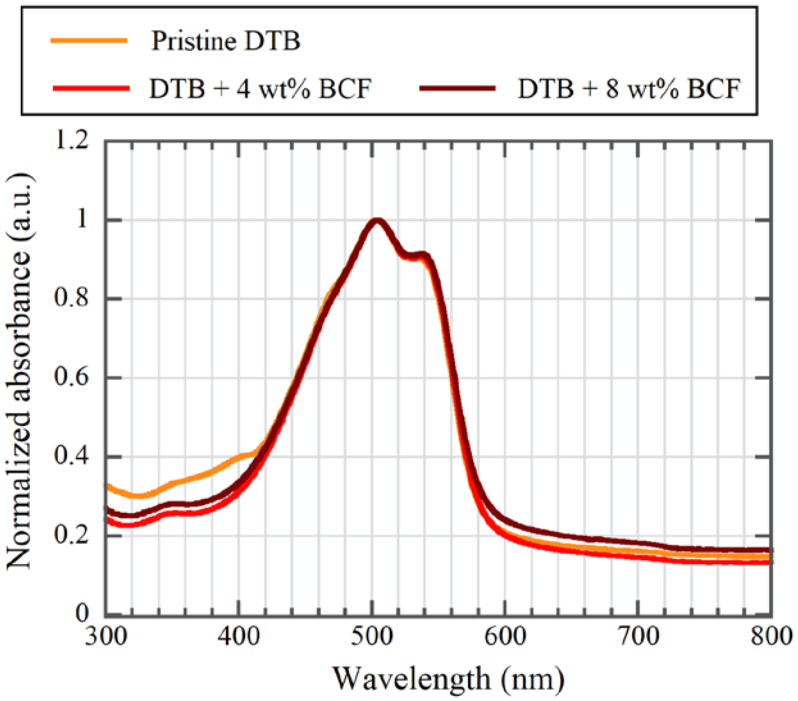

Figure 3-12. UV-Vis absorption spectra of high and low molecular weight DTB films without and with BCF-doping.

3.4 Conclusions

We fabricated mesoporous-type PSCs employing high and low molecule weight DTB copolymers as HTMs under nitrogen and measured the device performance in air. Devices

that were fabricated with high molecule weight DTB as an HTM had an initial PCE value of 3.05%. However, device performance gradually improved to 16.20% by oxygen-doping. After oxygen-doping was saturated, the superior molecular order of the high molecular weight DTB-based device yielded a higher PCE than the low molecular weight DTB-based device. When BCF (4.0 wt%) was added to the DTB, the initial PCE was 12.12% and improved to 16.89% by oxygen-doping. This value was the maximum PCE observed in this study. The BCF dopant caused this improvement in the initial device performance by increasing the carrier density of DTB.

References

1) S. Chen, P. Liu, Y. Hua, Y. Li, L. Kloo, X. Wang, B. Ong, W.-K. Wong and X. Zhu, ACS Appl. Mater. Interfaces, **9**, 13231-13239 (2017).
2) F. Zhang, C. Yi, P. Wei, X. Bi, J. Luo, G. Jacopin, S. Wang, X. Li, Y. Xian, S. M. Zakeeruddin and M. Grätzel, Adv. Energy Mater., **6**, 1600401 (2016).
3) J. Zhang, B. Xu, L. Yang, A. Mingorance, C. Ruan, Y. Hua, L. Wang, N. Vlachopoulos, M. Lira-Cantú, G. Boschloo, A. Hagfeldt, L. Sun and E. M. J. Johansson, Adv. Energy Mater., **7**, 1602736 (2017).
4) S. Paek, P. Qin, Y. Lee, K. T. Cho, P. Gao, G. Grancini, E. Oveisi, P. Gratia, K. Rakstys, S. A. Al-Muhtaseb, C. Ludwig, J. Ko and M. K. Nazeeruddin, Adv. Mater., **29**, 1606555 (2017).
5) X. Liu, X. Zheng, Y. Wang, Z. Chen, F. Yao, Q. Zhang, G. Fang, Z.-K. Chen, W. Huang and Z.-X. Xu, ChemSusChem, **10**, 2833-2838 (2017).
6) Y. C. Kim, T.-Y. Yang, N. J. Jeon, J. Im, S. Jang, T. J. Shin, H.-W. Shin, S. Kim, E. Lee, S. Kim, J. H. Noh, S. I. Seok and J. Sao, Energy Environ. Sci., **10**, 2109-2116 (2017).
7) Y. Liu, Q. Chen, H.-S. Duan, H. Zhou, Y. Yang, H. Chen, S. Luo, T.-B. Song, L. Dou, Z. Hong, and Y. Yang, J. Mater. Chem. A, **3**, 11940-11947 (2015).
8) K. Rakstys, S. Paek, P. Gao, P. Gratia, T. Marszalek, G. Grancini, K. T. Cho, K. Genevicius, V. Jankauskas, W. Pisula and M. K. Nazeeruddin, J. Mater. Chem. A, **5**, 7811-7815 (2017).
9) Y. Xue, Y. Wu and Y. Li, J. Power Sources, **344**, 160-169 (2017).
10) C. Huang, W. Fu, C.-Z. Li, Z. Zhang, W. Qiu, M. Shi, P. Heremans, A. K.-Y. Jen and H. Chen, J. Am. Chem. Soc., **138**, 2528-2531 (2016).
11) Z. Li, Z. Zhu, C.-C. Chueh, S. B. Jo, J. Luo, S.-H. Jang and A. K.-Y. Jen, J. Am. Chem. Soc., **138**, 11833-11839 (2016).
12) C. Chen, M. Cheng, P. Liu, J. Gao, L. Kloo and L. Sun, Nano Energy, **23**, 40-49 (2016).
13) G. Yang, Y.-L. Wang, J.-J. Xu, H.-W. Lei, C. Chen, H.-Q. Shan, X.-Y. Liu, Z.-X. Xu and G.-J. Fang, Nano Energy, **31**, 322-330 (2017).
14) Q. Zhu, X. Bao, J. Yu, D. Zhu, M. Qiu, R. Yang and L. Dong, ACS Appl. Mater. Interfaces, **8**, 2652-2657 (2016).
15) G.-W. Kim, J. Lee, G. Kang, T. Kim and T. Park, Adv. Energy Mater., **8**, 1701935 (2018).
16) H.-C. Liao, T. L. D. Tam, P. Guo, Y. Wu, E. F. Manley, W. Huang, N. Zhou, C. M. M. Soe, B. Wang, M. R. Wasielewski, L. X. Chen, M. G. Kanatzidis, A. Facchetti, R. P. H. Chang and T. J. Marks, Adv. Energy Mater., **6**, 1600502 (2016).
17) K. Kranthiraja, K. Gunasekar, H. Kim, A.-N. Cho, N.-G. Park, S. Kim, B. J. Kim, R.

Nishikubo, A. Saeki, M. Song and S.-H. Jin, Adv. Mater., **29**, 1700183 (2017).

18) B. Conings, L. Baeten, T. Jacobs, R. Dera, J. D'Haen, J. Manca and H.-G. Boyen, APL Mater., **2**, 081505 (2014).
19) J.-W. Lee, S. Park, M. J. Ko, H. J. Son and N.-G. Park, ChemPhysChem, **15**, 2595-2603 (2014).
20) P. Nagarjuna, K. Narayanaswamy, T. Swetha, G. H. Rao, S. P. Singh and G. D. Sharma, Electrochimica Acta, **151**, 21-26 (2015).
21) B. Cai, Y. Xing, Z. Yang, W.-H. Zhang and J. Qiu, Enargy Environ. Sci., **6**, 1480-1485 (2013).
22) G.-W. Kim, G. Kang, J. Kim, G.-Y. Lee, K. I. Kim, L. Pyeon, J. Lee and T. Park, Enargy Environ. Sci., **9**, 2326-2333 (2016).
23) J. Kim, G. Kim, T. K. Kim, S. Kwon, H. Back, J. Lee, S. H. Lee, H. Kang and K. Lee, J. Mater. Chem. A, **2**, 17291-17296 (2014).
24) W. Chen, X. Bao, Q. Zhu, D. Zhu, M. Qiu, M. Sun and R. Yang, J. Mater. Chem. C, **3**, 10070-10073 (2015).
25) E. Edri, S. Kirmayer, D. Cahen and G. Hodes, J. Phys. Chem. Lett., **4**, 897-902 (2013).
26) J. Lee, M. M. Byranvand, G. Kang, S. Y. Song, S. Song, G.-W. Kim and T. Park, J. Am. Chem. Soc., **139**, 12175-12181 (2017).
27) J. Liu, Q. Ge, W. Zhang, J. Ma, J. Ding, G. Yu, and J. Hu, Nano Res., **11**, 185-194 (2018).
28) A. Dubey, N. Adhikari, S. Venkatesan, S. Gu, D. Khatiwada, Q. Wang, L. Mohammad, M. Kumar and Q. Qiao, Sol. Energy Mater. Sol. C., **145**, 193-199 (2016).
29) T. Ye, J. Wang, W. Chen, Y. Yang and D. He, ACS Appl. Mater. Interfaces. **9**, 17923 (2017).
30) C. W. Koh, J. H. Heo, M. A. Uddin, Y.-W. Kwon, D. H. Choi, S. H. Im and H. Y. Woo, ACS Appl. Mater. Interfaces. **9**, 43846 (2017).
31) J. Luo, J. Xia, H. Yang, L. Chen, Z. Wan, F. Han, H. A. Malik, X. Zhu and C. Jia, Energy Environ. Sci., **11**, 2035-2045 (2018).
32) S. S. Reddy, V. M. Arivunithi, A. G. Sree, H. Kwon, J. Park, Y.-C. Kang, H. Zhu, Y.-Y. Noh and S.-H. Jin, Nano Energy, **58**, 284-292 (2019).
33) L. Zhang, C. Liu, J. Zhang, X. Li, C. Chun, Y. Tian, A. K.-Y. Jen and B. Xu, Adv. Mater. 30, 1804028 (2018).
34) Y. Nishihara, N. Onozawa-Komatsuzaki, H. Tachibana, M. Chikamatsu and Y. Yoshida, Ext. Abstr. Solid State Devices and Materials, 2019, p. 119.
35) H. Tachibana, N. Toda, N. Takada, M. Chikamatsu, and R. Azumi: Jpn. J. Appl. Phys. in

press.

36) P. Pingel, M. Arvind, L. Kölln, R. Steyrleuthner, F. Kraffert, J. Behrends, S. Janietz and D. Neher, Adv. Electron. Mater. **2**, 1600204 (2016).

Chapter IV

Effect of inserting passivation layer on the perovskite solar cell fabricated with donor-accepter copolymer as the hole transporting layer

4.1 Introduction

Perovskite solar cells (PSCs) have been vigorously studied due to the high device performance and the advantage that can prepare via solution process.[1-3] The device structure of PSCs generally consists of three layers: electron transporting layer, perovskite layer and hole transporting layer (HTL). Especially mesoporous type devices (Figure 4-1(a)), HTL properties and interface control play important roles in device performance. One of the characteristics required for hole transporting material (HTM) is high hole mobility. And also, atmospheric stability is important when HTL is located on the surface of the device. In addition, band diagrams should be matched between perovskite and HTM.

2,2',7,7'-tetrakis(N,N-di-p-methoxyphenylamine)-9,9'-spirobifluorene (Spiro-OMeTAD) has been widely employed as standard HTM. This HTM is often added with lithium bis(trifluoromethanesulfonyl) imide (Li-TFSI) when it is employed due to its low conductivity.[4),5)] However, Li-TFSI is hygroscopic and forms pinholes in the HTL. These features degrade the spiro-OMeTAD based device. In addition, spiro-OMeTAD itself is also expensive because of its complex molecular structure. For these reasons, alternative HTMs have been actively explored.

Many dopant-free HTM have been reported in both small molecule materials [6-10)] and conjugated polymers. [11-15)] Also, HTLs were employed tris(pentafluorophenyl)borane (BCF, Figure 4-1(b)) as a non-hygroscopic dopant to replace Li-TFSI have been reported.[16-19)] Conjugated polymers have been attempted adjusting energy levels due to side chain engineering.[11-13)] Thereby, band alignment with perovskite layer and atmospheric stability are improved. On the other hand, conjugated polymers have been employed for organic solar cells and organic thin film transistors. Conjugated polymers such as polyacetylene[20)] and poly(p-phenylene vinylene) were reported in the early stage. After that, polythiophene and its derivatives represented by poly(3-hexylthiophene-2,5-diyl)[21), 22)] were vigorously studied. And recently, many donor-acceptor (D-A) copolymers composed of donor and acceptor units have been synthesized.[23-26)]

In this study, we fabricated mesoporous type PSCs which were employed BCF doped D-A copolymer, poly[(2,5-bis(2-hexyldecyloxy)phenylene)-*alt*-(5,6-difluoro-4,7-di(thiophen-2-yl)benzo[*c*][1,2,5]-thiadiazole)] (PPDT2FBT,[17),27),28)] Figure 4-1(c)) as HTLs. And then, we measured *J-V* characteristics and the trend of device performance when D-A copolymer was employed as the HTL was investigated. In addition, the effectiveness of carrier recombination suppression by inserting passivation layer[29)] was examined.

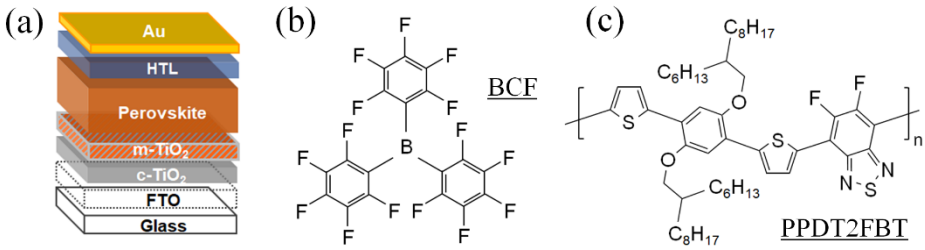

Figure 4-1. (a) The device structure of mesoporous type PSCs. Molecular structures of BCF (b) and PPDT2FBT (c).

4.2 Experimental procedure

The mesoporous-type PSC devices with a layered structure of fluorine-doping tin oxide (FTO) / compact-TiO_2 (c-TiO_2) / mesoporous-TiO_2 (m-TiO_2) / perovskite / HTL / Au is shown in Figure 4-1(a). FTO substrates were purchased from Nippon Sheet Glass (sheet resistance ≤ 10 Ω/sq). First, c-TiO_2 layers were formed on the FTO layer by spray pyrolysis. Titanium diisopropoxide bis(acetylacetonate) (Aldrich, 75 wt% in isopropanol) was further diluted with ethanol at 6 vol%. The diluted solution was sprayed at 400 °C and heated at 500 °C for 10 min. Next, m-TiO_2 layers were formed by spin coating a TiO_2 paste (Dyesol 18NRT) diluted with ethanol (14 wt%) at 2000 rpm for 30 s, which was then calcined at 120 °C for 15 min and 450 °C for 0.5 h. Perovskite layers were formed by anti-solvent method in a nitrogen-filled glove box. A precursor solution of CsI (42 μL of a 1.5 M stock solution in dimethyl sulfoxide (DMSO)), formamidine hydroiodide (FAI, 172 mg), methylamine hydrobromide (MABr, 22.4 mg), PbI_2 (507 mg), and $PbBr_2$ (73.4 mg) in 1 mL of a 4:1 volume ratio of *N*,*N*-Dimethylformamide (DMF) and DMSO was adjusted the composition $Cs_{0.05}FA_{0.79}MA_{0.16}PbI_{2.52}Br_{0.48}$. Perovskite films were deposited onto m-TiO_2 layers using a two-step spin-coating procedure. The first step was 1000 rpm for 10 s, and the second step was 6000 rpm for 20 s. To form smooth perovskite films, chlorobenzene (approximately 200 μL) was dropped onto the film during the second step at 15 s of the 20 s spin. The as-prepared films were heated at 40 °C for at least 5 min, 60 °C for 5 min, 70 °C for 5 min, and 100 °C for 1 h. We PPDT2FBT as shown in Figure 1(b). HTLs were fabricated in a nitrogen-filled glove box. In the case of PPDT2FBT devices, HTLs were deposited by spin coating of the dissolved PPDT2FBT in chlorobenzene (7.5 mg mL^{-1}). BCF (Figure 1(c)) was added to the PPDT2FBT solution as needed. Substrates and PPDT2FBT solution were preheated at 80 °C on a hot plate. Finally, Au electrodes were formed by thermal evaporation under vacuum at 5.0×10^{-4} Pa. The measured film thickness of each layer is as follows: FTO (710 nm) / TiO_2 (180 nm) / Perovskite (550 nm) / PPDT2FBT (30 nm) / Au (50 nm). In this

device, the film thickness of PPDT2FT layer less than 50 nm. This value is sufficiently thin as HTL.

J–V measurements of the devices under AM1.5G solar simulator illumination (Wacom WXS-80C-3 with a 300 W Xe lamp and an AM 1.5 filter) were performed with a DC voltage/current source monitor (Advantest R6243) in air at room temperature without encapsulation. For all measurements, devices were equipped with a 0.119 cm^2 metal aperture to define the active area. Device samples were kept in a desiccator in which humidity was controlled at < 5% relative humidity. During measurement procedures, samples were exposed to room air.

The ultraviolet-visible (UV-Vis) absorption spectra of PPDT2FBT films on quartz substrates were recorded using a Shimadzu UV-3600 UV-vis-NIR spectrophotometer.

4.3 Results and discussion

First, *J-V* curves obtained from mesoporous type devices which were employed spiro-OMeTAD and PPDT2FBT as HTLs are shown in Figure 4-2. And, measured device characteristics are shown in Table 4-1. Also, PCE histograms and plotted average *J-V* characteristic values are shown in Figure 4-3. Maximum PCE of spiro-OMeTAD based devices was recorded at 18.5% in the device fabrication conditions of this study. On the other hand, the fill factor (FF) of PPDT2FBT based devices was low due to distorted *J-V* curves. Therefore, the PCE of those devices was less than 15%. Thickness of PPDT2FBT layer was 30 to 50 nm. This value was thin enough for the HTL. Measured series resistance values were not significantly higher. And also, the ESR measurement results (Figure 4-4) show that the carrier concentration of PPDT2FBT increased with the addition of BCF. From these results, we infer that the conductivity of PPDT2FBT layers was sufficient.

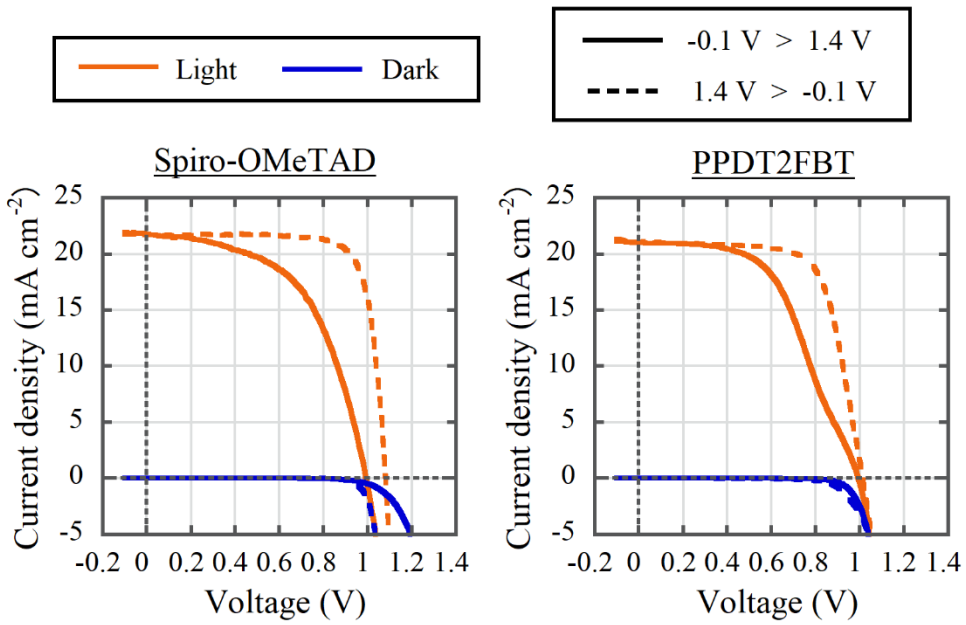

Figure 4-2. *J-V* curves of spiro-OMeTAD and PPDT2FBT based devices.

Table 4-1. *J-V* characteristic values of spiro-OMeTAD and PPDT2FBT based devices. (a) Mean ± standard deviation. (b) Values from Figure 4-2.

HTM	J_{sc} [mA cm^{-2}]	V_{oc} [V]	FF	PCE [%]	Rs [Ωcm^2]
Without passivation					
Spiro-OMeTAD	21.50 ± 0.18[a] (21.66)[b]	1.06 ± 0.01 (1.08)	0.75 ± 0.03 (0.79)	17.17 ± 0.87 (18.52)	5.74 ± 0.62 (4.76)
PPDT2FBT	20.64 ± 0.21 (21.05)	0.99 ± 0.01 (1.01)	0.67 ± 0.02 (0.70)	13.71 ± 0.59 (14.93)	4.92 ± 0.30 (4.53)

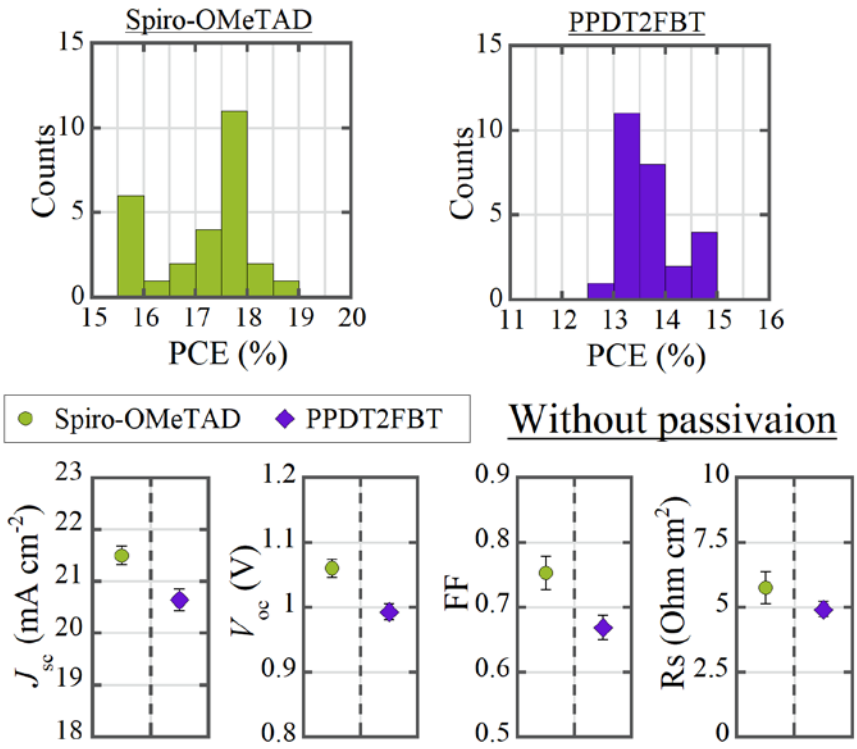

Figure 4-3. PCE histograms and plotted average *J-V* characteristic values from spiro-OMeTAD and PPDT2FBT based devices without passivation layers.

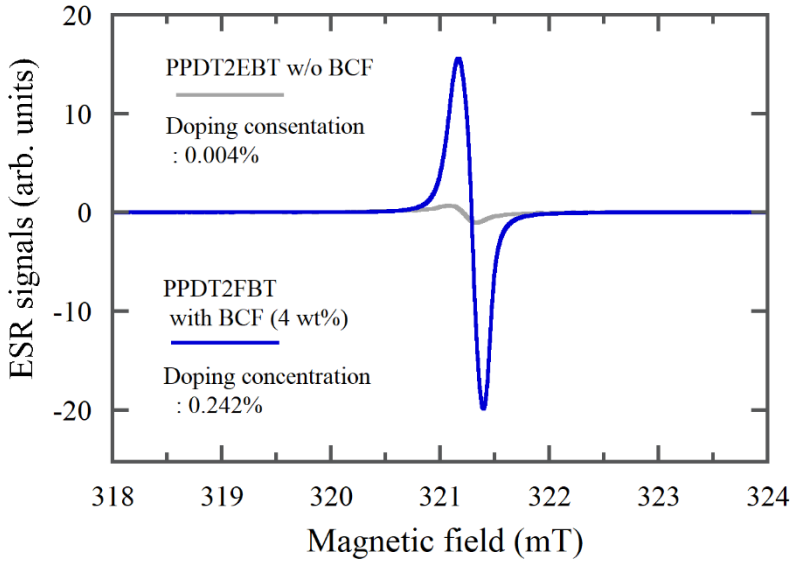

Figure 4-4. ESR spectrum of PPDT2FBT films with and without BCF doping.

Next, photoelectron yield spectroscopy (PYS) and ultraviolet-visible (UV-Vis) spectroscopy were performed on single layer samples of both HTMs and perovskite (Figure 4-5(a),(b)). The plotted band diagram from these results are shown in Figure 4-5(c). Highest

occupied molecular orbital (HOMO) level of PPDT2FBT was higher than that of spiro-OMeTAD. We thought that carrier recombination might have occurred in the interface between perovskite and PPDT2FBT layers because of the conduction band (CB) of perovskite was close to the HOMO level of PPDT2FBT. To confirm this consideration, we verified the effect of the passivation layer for suppress carrier recombination.

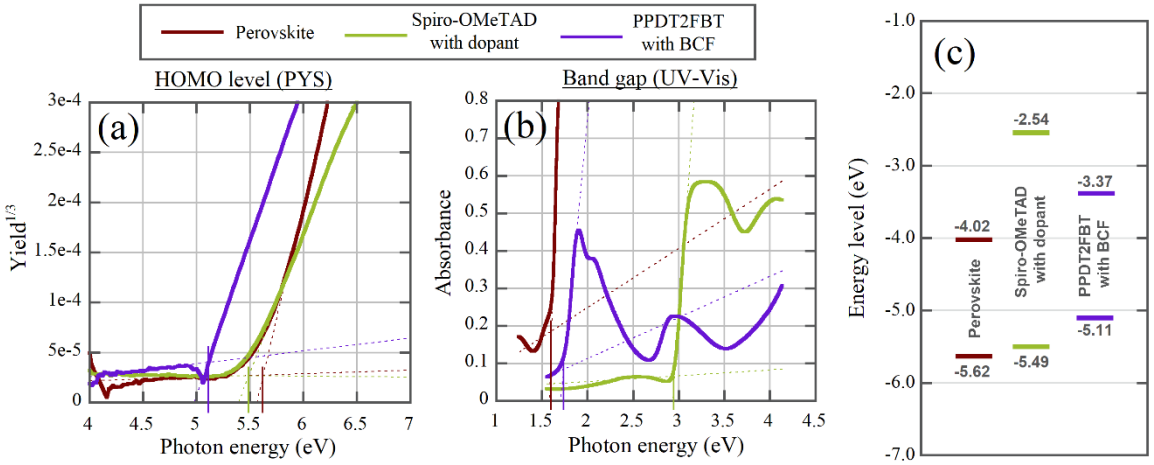

Figure 4-5. HOMO and VB levels were obtained by PYS (a) and optical band gaps were obtained by UV-Vis spectroscopy (b) from single layer samples of both HTMs and perovskite. (c) The plotted band diagram from these results.

Passivation layers were formed by the method proposed Co *et al.*[29] In this method, passivation layers were formed by reacting 2-propanol solution of formamidinium bromide (FABr) with PbI_2 remaining on the perovskite surface. This formed passivation layers were additional perovskite layers with compositional gradient. By FABr solution treatment, surface PbI_2 was removed and added $FAPbBr_{3-x}I_x$ layer functioned as a carrier recombination suppressing layer. X-ray diffraction spectra for mesoporous type devices with and without FABr solution treatment were shown in Figure 4-6. In the device treated with FABr solution, the peak corresponding to PbI_2 was not observed. Therefore, the formation of the passivation layer can be expected to have been performed sufficiently.

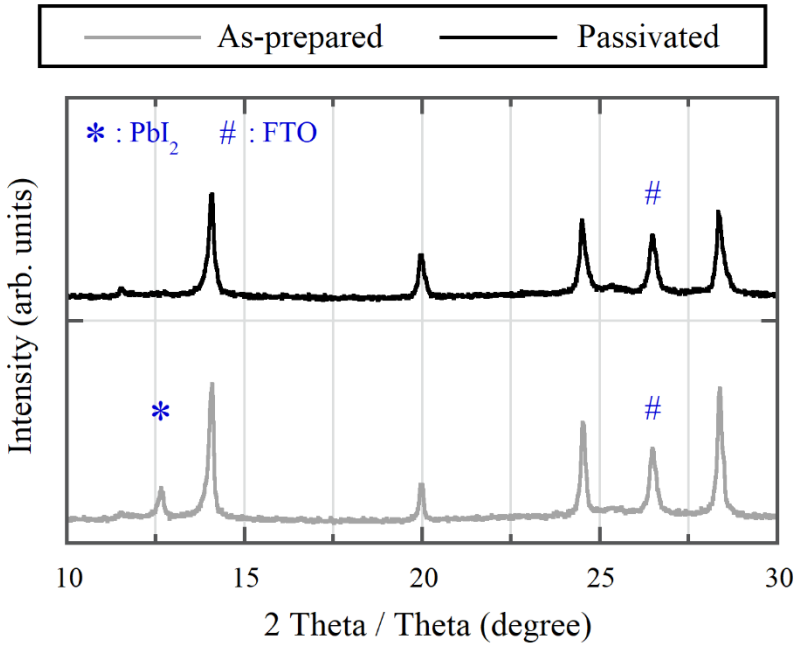

Figure 4-6. XRD spectrum of mesoporous type PSCs with and without FABr solution treatment on perovskite layers.

J-V curves obtained from mesoporous type devices with FABr solution treatment are shown in Figure 4-7. And, measured device characteristics are shown in Table 4-2. Also, PCE histograms and average of *J-V* characteristic values are shown in Figure 4-8. In the case of inserting the passivation layer for the spiro-OMeTAD based device, its open circuit voltage (V_{oc}) was risen up to 1.15V. This trend was similar to the previous study.[29] On the other hand, PCE did not improve because the FF and the short circuit current density (J_{sc}) dropped slightly. Increase in V_{oc} and decrease in J_{sc} could be confirmed even in the PPDT2FBT based device. In the case of inserting the passivation layer for the PPDT2FBT based device, the FF greatly improved to 0.81. As a result, the PCE risen up to 17.0%.

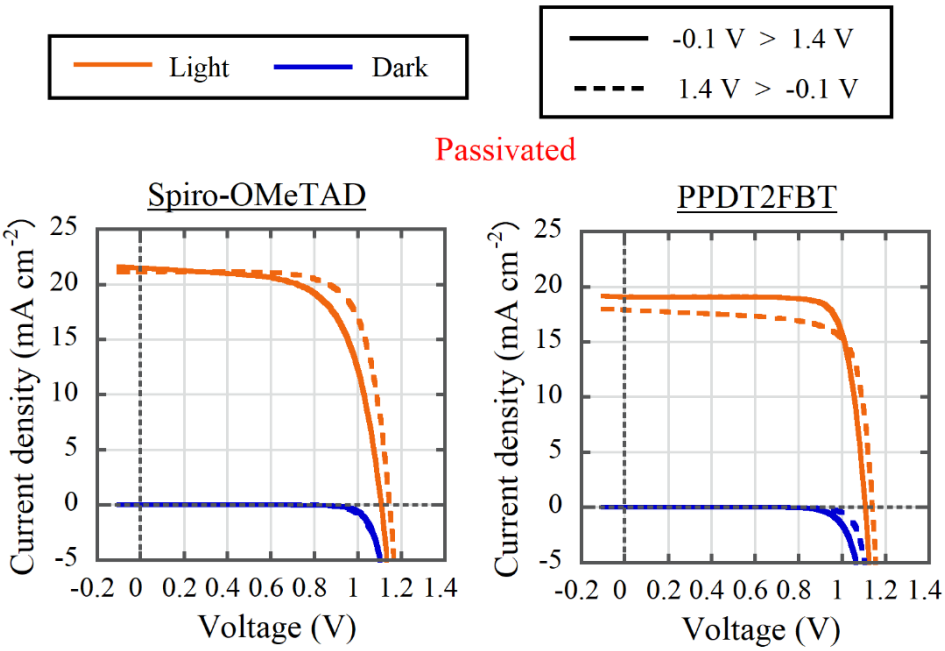

Figure 4-7. *J-V* curves of spiro-OMeTAD and PPDT2FBT based devices with inserting passivation layers.

Table 4-2. *J-V* characteristic values of spiro-OMeTAD and PPDT2FBT based devices with inserting passivation layers (a) Mean ± standard deviation. (b) Values from Figure 4-7.

HTM	J_{sc} [mA cm^{-2}]	V_{oc} [V]	FF	PCE [%]	Rs [Ωcm^2]
			With passivation		
Spiro-OMeTAD	20.88 ± 0.42[a] (21.13)[b]	1.13 ± 0.02 (1.15)	0.69 ± 0.03 (0.73)	16.30 ± 0.90 (17.78)	3.62 ± 0.20 (3.39)
PPDT2FBT	19.73 ± 0.48 (19.08)	1.07 ± 0.02 (1.11)	0.76 ± 0.03 (0.81)	16.12 ± 0.53 (17.00)	2.96 ± 0.25 (2.69)

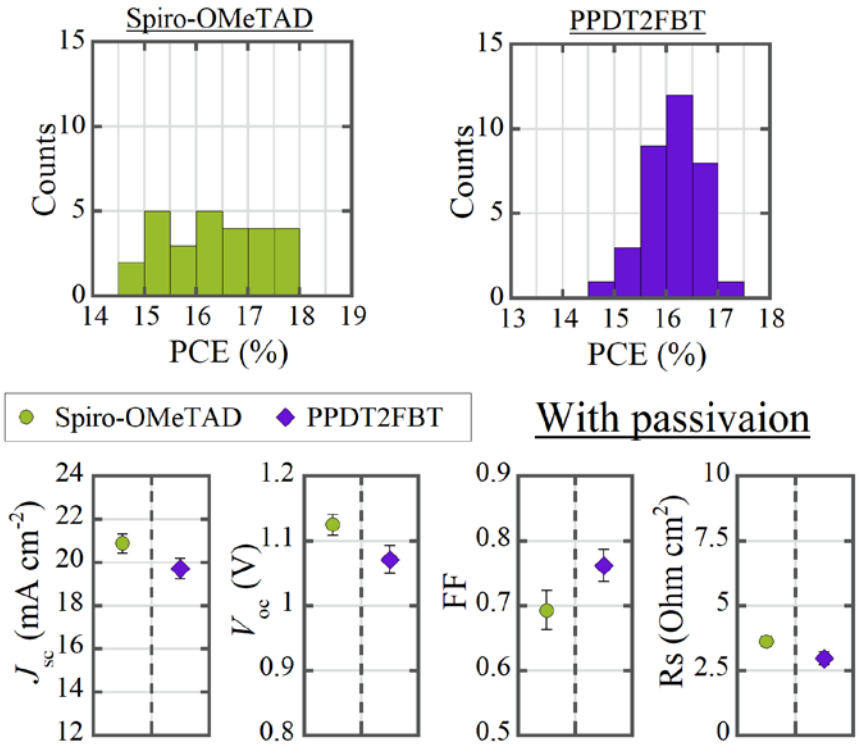

Figure 4-8. PCE histograms and plotted average *J-V* characteristic values from spiro-OMeTAD and PPDT2FBT based devices with inserting passivation layers.

The sample reproducing passivation layer was prepared by reacting FABr solution to PbI_2 monolayer film. PYS and UV-Vis spectroscopy were performed on reproduction sample and perovskite (Figure 4-9(a),(b)). The plotted band diagram from these results are shown in Figure 4-9(c). The valence band (VB) level of the sample that reproduces passivation layer slightly lower than that of the perovskite sample. By inserting the interlayer which was low VB level, the recombination was suppressed in interface between perovskite and PPDT2FBT layers. As a result, the FF after inserting passivation layer was improved. In Figure 4-10, the arrows indicate the recombination process of electrons. It is suggested that the inserting of passivation layer that suppresses recombination is important in D-A copolymers with higher HOMO levels compared to the spiro-OMeTAD.

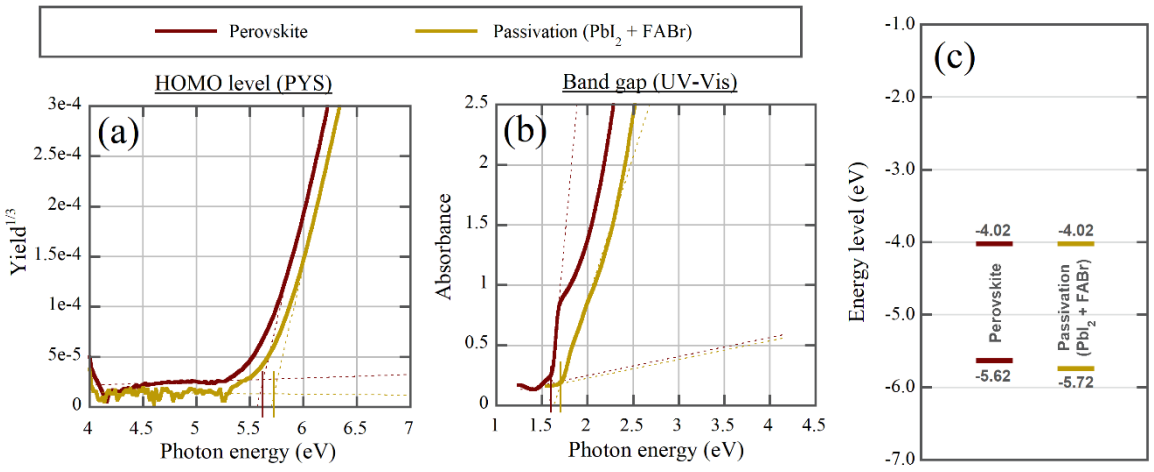

Figure 4-9. HOMO and VB levels were obtained by PYS (a) and optical band gaps were obtained by UV-Vis spectroscopy (b) from single layer samples of reproducing passivation and perovskite. (c) The plotted band diagram from these results.

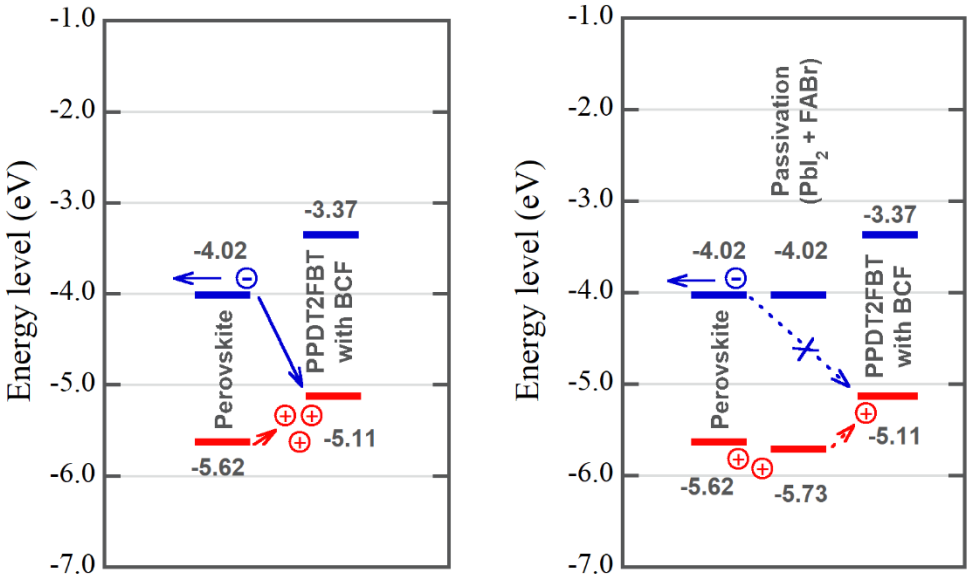

Figure 4-10. Inferred charge recombination mechanism in this study.

Finally, *J-V* curves of the optimized PPDT2FBT based device inserting passivation layer are shown in Figure 4-11, and *J-V* characteristic values are shown in Table 4-3. The PCE was recorded 18.4% comparable to spiro-OMeTAD based devices. This value was maximum PCE for PPDT2FBT based devices in this study.

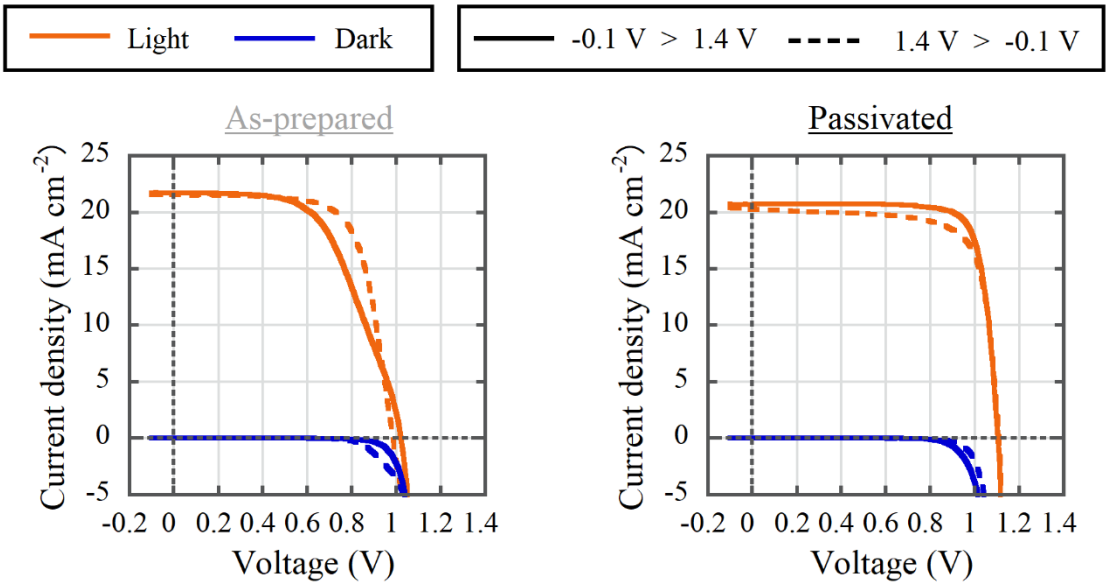

Figure 4-11. *J-V* curves of PPDT2FBT based devices with and without passivation layers.

Table 4-3. *J-V* characteristic values of PPDT2FBT based devices with and without passivation layers. Values from Figure 4-11.

J_{sc} [mA cm^{-2}]	V_{oc} [V]	FF	PCE [%]	Rs [Ωcm^2]
Without passivation				
21.53	0.98	0.70	14.81	3.31
With passivation				
20.69	1.10	0.81	18.40	2.07

4.4 Conclusions

In conclusion, we attempted suppressing carrier recombination by inserting the passivation layer which was formed FABr solution treatment. For the PPDT2FBT based device, the FF was greatly improved and PCE was increased by FABr solution treatment. The VB level of passivation layer was slightly lower than that of perovskite layer. For that reason, the carrier recombination at the Perovskite-PPDT2FBT interface was suppressed by inserting the interlayer which was low VB level. For the optimized PPDT2FBT based devices, the PCE was recorded 18.4% comparable to spiro-OMeTAD based devices.

References

1) A. Kojima, K. Teshima, Y. Shirai, and T. Miyasaka, J. Am. Chem. Soc. 2009, 131, 6050.
2) M. M. Lee, J. Teuscher, T. Miyasaka, T. N. Murakami and H. J. Snaith, Science 2012, 338, 643.
3) N. J. Jeon, J. H. Noh, W. S. Yang, Y. C. Kim, S. Ryu, J. Seo and S. I. Seok, Nature 2015, 517, 476.
4) A. Abate, T. Leijtens, S. Pathak, J. Teuscher, R. Avolio, M. E. Errico, J, Kirkpatrik, J. M. Ball, P. Docampo, I. McPherson and H. J. Snaith, Phys. Chem. Chem. Phys. 2013, 15, 2572.
5) P. Docampo, S. Guldin, T. Leijitens, N. K. Noel, U. Steiner and H. J. Snaith, Adv. Mater. 2014, 26, 4013.
6) S. Chen, P. Liu, Y. Hua, Y. Li, L. Kloo, X. Wang, B. Ong, W.-K. Wong and X. Zhu, ACS Appl. Mater. Interfaces 2017, 9, 13231.
7) F. Zhang, C. Yi, P. Wei, X. Bi, J. Luo, G. Jacopin, S. Wang, X. Li, Y. Xian, S. M. Zakeeruddin and M. Grätzel, Adv. Energy Mater. 2016, 6, 1600401.
8) J. Zhang, B. Xu, L. Yang, A. Mingorance, C. Ruan, Y. Hua, L. Wang, N. Vlachopoulos, M. Lira-Cantú, G. Boschloo, A. Hagfeldt, L. Sun and E. M. J. Johansson, Adv. Energy Mater. 2017, 7, 1602736.
9) S. Paek, P. Qin, Y. Lee, K. T. Cho, P. Gao, G. Grancini, E. Oveisi, P. Gratia, K. Rakstys, S. A. Al-Muhtaseb, C. Ludwig, J. Ko and M. K. Nazeeruddin, Adv. Mater. 2017, 29, 1606555.
10) X. Liu, X. Zheng, Y. Wang, Z. Chen, F. Yao, Q. Zhang, G. Fang, Z.-K. Chen, W. Huang and Z.-X. Xu, ChemSusChem 2017, 10, 2833.
11) G.-W. Kim, J. Lee, G. Kang, T. Kim and T. Park, Adv. Energy Mater. 2018, 8, 1701935.
12) H.-C. Liao, T. L. D. Tam, P. Guo, Y. Wu, E. F. Manley, W. Huang, N. Zhou, C. M. M. Soe, B. Wang, M. R. Wasielewski, L. X. Chen, M. G. Kanatzidis, A. Facchetti, R. P. H. Chang and T. J. Marks, Adv. Energy Mater. 2016, 6, 1600502.
13) G.-W. Kim, G. Kang, J. Kim, G.-Y. Lee, K. I. Kim, L. Pyeon, J. Lee and T. Park, Energy Environ. Sci. 2016, 9, 2326.
14) K. Kranthiraja, K. Gunasekar, H. Kim, A.-N. Cho, N.-G. Park, S. Kim, B. J. Kim, R. Nishikubo, A. Saeki, M. Song and S.-H. Jin, Adv. Mater. 2017, 29, 1700183.
15) W. Chen, X. Bao, Q. Zhu, D. Zhu, M. Qiu, M. Sun and R. Yang, J. Mater. Chem. C 2015, 3, 10070.
16) T. Ye, J. Wang, W. Chen, Y. Yang and D. He, ACS Appl. Mater. Interfaces 2017, 9, 17923.
17) C. W. Koh, J. H. Heo, M. A. Uddin, Y.-W. Kwon, D. H. Choi, S. H. Im and H. Y. Woo, ACS Appl. Mater. Interfaces 2017, 9, 43846.

18) J. Luo, J. Xia, H. Yang, L. Chen, Z. Wan, F. Han, H. A. Malik, H. Zhu and C. Jia, Energy Environ. Sci. 2018, 11, 2035.
19) S. S. Reddy, V. M. Arivunithi, V. G. Sree, H. Kwon, J. Park, Y.-C. Kang, H. Zhu, Y.-Y. Noh and S.-H. Jin, Nano Energy 2019, 58, 284.
20) H. Shirakawa, E. J. Louis, A. G. MacDiarmid, C. K. Chiang and A. J. Heeger, J. Chem. Soc., Chem. Comm. 1977, 578.
21) R. D. McCullough and R. D. Lowe, J. Chem. Soc., Chem. Comm. 1992, 70
22) T.-A. Chen and R. D. Rieke, J. Am. Chem. Soc. 1992, 114, 10087.
23) I. Osaka, G. Sauvé, R. Zhang, T. Kowalewski and R. D. McCullough, Adv. Mater. 2007, 19, 4160.
24) I. Osaka, R. Zhang, B. Sauvé, D.-M. Smilgies, T. Kowalewski and R. D. McCullough, J. Am. Chem. Soc. 2009, 131, 2521.
25) N. Blouin, A. Michaud and M. Leclerc, Adv. Mater. 2007, 19, 2295.
26) Y. Liang, Z. Xu, J. Xia, S.-T. Tsai, Y. Wu, G. Li, C. Ray and L. Yu, Adv. Mater. 2010, 22, E135.
27) M. A. Uddin, Y. H. Lee, S. Xu, S. Y. Park, T. Kim, S. Song, T. L. Nguyen, S.-J. Ko, S. Hwang, J. Y. Kim and H. Y. Woo, ACS. Chem. Mater. 2015, 27, 5997
28) H. Kang, M. A. Uddin, C. Lee, K.-H. Kim, T. L. Nguyen, W. Lee, Y. Li, C. Wang, H. Y. Woo and B. J. Kim, J. Am. Chem. Soc. 2015, 137, 2359.
29) K. T. Cho, S. Paek, G. Grancini, C. Roldán-Carmona, P. Gao, Y. Lee and M. K. Nazeeruddin, Energy Environ. Sci. 2017, 10, 621.

Chapter V

Summary

Summary

In this doctoral study, we focused hole transporting mate materials (HTMs) and interface control methods, and conducted research as follows.

In Chapter I, we outlined current state of perovskite solar cells (PSCs).

In Chapter II, we studied on influence of O_2 plasma treatment for NiO_x layers in PSCs. This hydrophilic treatment made it possible to form the perovskite layer on the NiO_x layer by the spin coating used precursor solution. We have revealed that NiO_x films are sensitivity to O_2 plasma treatment. When treating too strong, it can be assumed that the electronic state of NiO_x layers were negatively affected. The power conversion efficiency (PCE) was reached to 12.3% in the case of optimized treatment was performed.

In Chapter III, we studied on influence of p-type dopants such as oxygen and tris(pentafluorophenyl)borane (BCF) for organic polymer hole transporting layers (HTLs) in mesoporous type PSCs. Mesoporous type devices which were employed dithiophene-benzene (DTB) copolymer without dopant as HTM were prepared under nitrogen environment. And then, these devices were measured *J-V* characteristics in air. As a result, initial PCE was shown very low value of 2.98% at 5 hours after exposed to the atmosphere. However, the device performance was gradually improved by keeping in dry air. And PCE was reached to 16.15% at 1 week after keeping. The cause of this phenomenon was guessed to be that oxygen in the atmosphere diffused into HTLs. It is considered that the carrier density increased due to the doping effect of oxygen and resistance of HTLs are decreased. The initial PCE was improved to 12% by the addition of BCF to HTLs because sufficient carrier density was obtained in initial stage. Further, the PCE was reached 16.89% by combining oxygen doping.

In Chapter IV, we studied on effect of charge recombination suppression due to inserting the passivation layer. When BCF doped poly[(2,5-bis(2-hexyldecyloxy)phenylene)-*alt*-(5,6-difluoro-4,7-di(thiophen-2-yl)benzo[*c*][1,2,5]-thiadiazole)] (PPDT2FBT) was employed as HTM, the *J-V* curve was distorted and the fill factor (FF) was lower than when employed 2,2',7,7'-tetrakis(N,N-di-p-methoxyphenylamine)-9,9'-spirobifluorene (Spiro-OMeTAD). The highest occupied molecular orbital (HOMO) level of PPDT2FBT is higher than that of Spiro-OMeTAD. Therefore, charge recombination may have occurred on the HTL side because the conduction band level of the perovskite layer is close to the HOMO level of PPDT2FBT. To suppress charge recombination, we tried to insert the passivation layer which was formed by reacting the remaining PbI_2 with formamidinium bromide dissolved in 2-

propanol. As the result, the FF and the PCE were improved in the PPDT2FBT-based device by inserting the passivation layer. The valence band level of the passivation layer was slightly lower than that of original perovskite layer. For that reason, the passivation layer separates the conduction band level of the perovskite layer from the HOMO level of the PPDT2FBT layer. In addition, it is guessed that the frequency of charge recombination was reduced by making the flow of holes slightly gentler. The PCE of passivated PPDT2FBT device which was optimized composition of perovskite layer was reached to 18.4% comparable to Spiro-OMeTAD based device.

Finally, we consider the future prospects as follows. PCE of inverted planar type devices is lower than that of mesoporous type devices at the moment. However, inverted planar type devices possess more commercial advantages. Therefore, controlling wettability on the HTL of inverted planar type device is important when performing mass production using printing methods. In this doctoral study, it was found that increasing the carrier density by p-type doping and suppressing charge recombination by inserting the passivation layer were effective in polymer HTMs. By utilizing these results, it is expected that better devices will be obtained in the future.

List of publications

Chapter II

Yoshihiko Nishihara, Masayuki Chikamatsu, Said Kazaoui, Tetsuhiko Miyadera, and Yuji Yoshida, Influence of O2 plasma treatment on NiO_X layer in perovskite solar cells., *Japanese Journal of Applied Physics* 57, 04FS07-1-4 (2018).

Chapter III

Yoshihiko Nishihara, Nobuko Onozawa-Komatsuzaki, Hiroaki Tachibana, Masayuki Chikamatsu, Yuji Yoshida, Influence of p-type doping on perovskite solar cells fabricated with Dithiophene-benzene copolymer as the hole transporting layer., *Japanese Journal of Applied Physics*, (2020)[in press]

Chapter IV

Yoshihiko Nishihara, Nobuko Onozawa-Komatsuzaki, Zou Xiangtao, Kazuhiro Marumoto, Masayuki Chikamatsu, Yuji Yoshida, Effect of inserting passivation layer on the perovskite solar cell fabricated with donor-accepter copolymer as the hole transporting layer., in preparation.

Acknowledgments

This work was supported by the New Energy and Industrial Technology Development Organization (NEDO). In Chapter II, the authors would like to thank Dr. H. Tampo, Mr. T. Sugita, and Dr. Sayama for their help with NiOx film preparation and characterization.